



LUNDS UNIVERSITET

MASTER THESIS

Magnetization dynamics in nanorings

Author:
Simon YDMAN

Supervisor:
Claudio VERDOZZI

*A thesis submitted in fulfilment of the requirements
for the degree of Master of Physics*

in the

Division of Mathematical Physics

June 2015

“We dance round in a ring and suppose, but the secret sits in the middle and knows.”

Robert Frost

LUNDS UNIVERSITET

Abstract

Faculty of Science

Division of Mathematical Physics

Master of Physics

Magnetization dynamics in nanorings

by Simon YDMAN

This thesis investigates numerically the out of equilibrium properties of quantum rings with magnetic impurities, using the periodic Anderson model (PAM). The model is a simple template for the discussion of the physics of regular arrays of rare-earth impurities in metallic hosts. The system considered is a quantum ring consisting of up to six sites, each of whom are connected to an Anderson impurity site. The dynamical properties of this system are investigated numerically using exact diagonalization and Lanczos adapted time evolution. Two different schemes are used to perturb the system: a magnetic field piercing the ring and a local Zeeman interaction at one of the conduction sites. Comparisons are made with a ring without impurities, and it is shown that for very strong onsite interaction and/or very weak hybridization between the conduction sites and the impurity sites, the physics of a ring without impurities is recovered. Furthermore, a Doniach-type phase diagram in the presence of persistent currents, is provided where it is shown that the Kondo regime is reached for smaller values of the hybridization parameter when a magnetic field piercing the ring is present. The Doniach phase diagram is discussed in connection with persistent currents and entanglement. Preliminary results for the Zeeman field suggests a non trivial interplay between charge and spin currents, and RKKY and Kondo-like couplings.

Acknowledgements

I would first of all like to thank supervisor Claudio, who has given a lot of his time to discuss anything and everything concerning this thesis project. Thank you for tolerating my sometimes childish stubbornness, and for your great sense of humor. Furthermore, I would like to thank Miroslav, and Emil, for all their help.

All of the student in the master's room ought to be thanked for making this project a pleasant experience. A special thanks goes to Kevin for kindly lending me his exceptional grammar skills. The amount of fun, or at least cake, has increased quadratically since you joined.

A big thanks to all of the people at the division of Mathematical physics, you all make for a very nice atmosphere.

At last, I would like to thank Åsa for moral support, and for punching me whenever I couldn't get the physics out of my head.

Contents

Abstract	ii
Acknowledgements	iii
List of Figures	v
1 Introduction	1
1.1 The Kondo effect	3
1.1.1 The Anderson model	4
1.2 Quantum rings	6
1.2.1 Peierls substitution	7
1.2.2 Quantum rings in the periodic Anderson model	8
1.3 Computational considerations	9
2 Method	11
2.1 Defining the system	12
2.2 Groundstate calculation	14
2.3 Time evolution	14
2.4 Operators	18
2.4.1 Current	18
2.4.2 Spin correlations	20
2.5 Entanglement and concurrence	21
3 Results	23
3.1 Comparison of computational techniques	23
3.2 One-dimensional quantum rings	28
3.3 Quantum rings in the periodic Anderson model	29
3.3.1 Local magnetic field	33
4 Conclusions and Outlook	37
Bibliography	39

List of Figures

1.1	Periodic Anderson model ring	2
1.2	Resistance at low temperatures (from Kondos original paper)	4
2.1	Qutip tree-diagram	12
2.2	Illustrative picture of the state movement in the Hilbert space.	16
2.3	Currents in the PAM	19
3.1	Comparison of computational techniques 1	24
3.2	Comparison of computational techniques 2	26
3.3	Relative error of t-DMRG	27
3.4	Steady state and TE of 1D ring	28
3.5	Steady state and TE of 1D ring at half filling.	29
3.6	Spin-spin correlations reproduced from literature	30
3.7	Doniach phase diagram in the (V, ϕ) -plane	31
3.8	Persistent current of PAM ring	32
3.9	Entanglement of PAM ring	33
3.10	Spin-spin correlations after magnetic pulse.	34
3.11	Charge and spin-currents after magnetic pulse	35
3.12	Spin-spin correlations for different sites, after magnetic pulse	36

Chapter 1

Introduction

The past 50 years have seen increasingly rapid advances in computer technology. The increases in computational power have really been exponential, elegantly highlighted by Moore's Law [1]. In 1965 Moore made the prediction that the number of transistors in dense integrated circuits would double every two years, and his prediction has held true until today. However, the breakdown of Moore's law is inevitable as the decrease of transistor sizes cannot go on indefinitely. This breakdown is expected to occur in the near future [2], and as a consequence a lot of effort has been put into research of alternative methods of increasing computational power. One of the more spectacular areas of research in those matters is quantum computing. Quantum computers are in short like regular computers, except that they make use of quantum mechanical phenomena, such as superposition and entanglement, to speed up certain computations. Quantum computers are expected to be much faster at performing specific tasks, for example the factorization of large numbers [3], but the experimental realization of a quantum computer is far away. Another emerging field, which also proposes a revolutionary approach to regular electronics, is spintronics (or magnonics). It suggests that instead of electron density waves, electron spin waves could be used as means of transporting information.

Spintronics would have several advantages over regular electronics. It is for example expected that spintronic devices would generate much less heat than regular electronic devices [4]. Another argument that is put forth is that spin waves have much shorter wavelength which would allow for smaller devices. Furthermore, since the properties of spin waves are different from those of density waves, it could be possible to create devices that are impossible in regular electronics. Spintronics is a relatively young field and the full potential of spin dependent devices is far from fathomed. The appearance of spintronics, along with the progress in the controlled manufacturing of nanodevices,

has brought a renewed interest to a much older phenomenon, namely the Kondo effect [5].

This thesis will examine the Kondo effect and magnetization dynamics in quantum rings. The system considered is a quantum ring consisting of six sites, each connected to a magnetic orbital which is described by an Anderson impurity site (see Fig. 1.1). The groundstate properties of this system have been investigated in previous studies [6–8], but nothing has been done for the dynamical aspects, and that is what this project is about. The study is numerical, and the computer program that was used for the simulation of the system was build as part of the project.

The program was developed in Python, and was tested using a time-dependent Density Matrix Renormalization Group (t-DMRG) program (source code from [9]). The t-DMRG program was interfaced in Python for easy use in Hubbard/Anderson type of systems. Furthermore, the interfaced t-DMRG code was used as a benchmark for a novel many-body approximation method developed in a different, larger scale project. Our collaboration and co-authorship in that project (a paper will be submitted in the next few weeks) was provided during the thesis work and can be seen as an additional, but secondary, subproject of the thesis. Consequently, we find it appropriate and informative to present some results on the topic here.

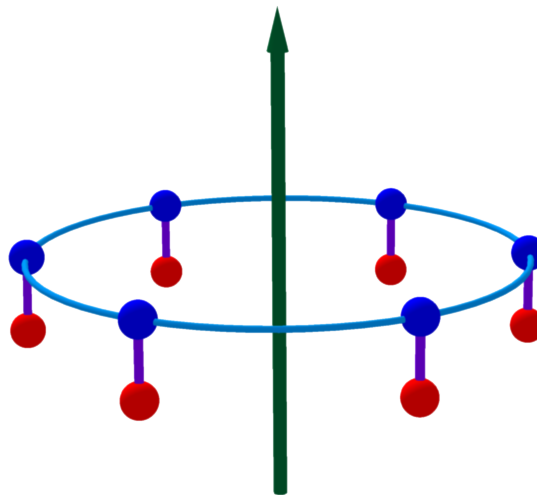


FIGURE 1.1: Schematic figure of the system considered in this thesis. The blue sites represent the conduction sites. They are connected to each other through a hopping term which can be altered by a magnetic field piercing the ring. The red sites correspond to the Anderson impurity sites with which the conduction electrons can interact.

The thesis is composed of four chapters. Chapter 1 (this chapter) gives an introduction to the field of Kondo physics, spin interactions and quantum rings. It will also provide

a short overview of the computational methods connected to the thesis project. The second chapter (2) explains the numerical method of the developed computer program and the observables used to analyze the systems investigated. The third chapter (3) is concerned with the results. It starts with a comparison between exact diagonalization (used in the developed computer program), time dependent density matrix renormalization group, two commonly used many-body approximation (MBA) methods, and a new MBA method. Then results for regular 1D rings (without magnetic impurities) will be presented, followed by results for periodic Anderson model rings. The final chapter (4) concludes the thesis, and provides an outlook for further studies.

1.1 The Kondo effect

The Kondo effect was discovered in the 1930s when de Haas *et al.* [10] made the mind-boggling discovery that for some metals, as the temperature is lowered, the resistance reaches a minimum and increases logarithmically as $T \rightarrow 0$. It was known at that time that the resistance in a material was affected by the scattering of conduction electrons against static impurities, lattice imperfections, and vibrations (phonons). According to the theory at that time, if temperature is lowered, the lattice vibrations will diminish and the resistance should saturate at a specific value, depending on the amount of impurities and lattice imperfections. The findings of de Haas *et al.* contradicted this picture and made it clear that there were missing pieces in the theory of resistance.

In the beginning of the 60's it was recognized that this effect was related to the level of magnetic impurities in the metal, and in 1964 Jun Kondo was able to show that the effect was due to spin exchange interactions between conduction electrons and unpaired electrons in magnetic orbitals [11]. The Hamiltonian that Kondo used was composed of two parts, a regular Bloch Hamiltonian describing the electron sea, and an interaction Hamiltonian

$$H_K = J \vec{S} \cdot \vec{s}(\vec{r}). \quad (1.1)$$

Here \vec{S} refers to the spin of the impurity and $\vec{s}(\vec{r})$ to the spin of the conduction electrons at the impurity site \vec{r} . Using third order perturbation theory, Kondo was able to reproduce the logarithmic behavior of the resistance seen in experiments (see Fig. 1.2).

In the Kondo Hamiltonian J is a positive constant which implies that the coupling between the impurity and the conduction electrons is anti-ferromagnetic. The physical reason for the positive J has to do with the nature of the spin-flip processes that cause the effect. Kondo himself used it as a parameter because it was necessary to reproduce

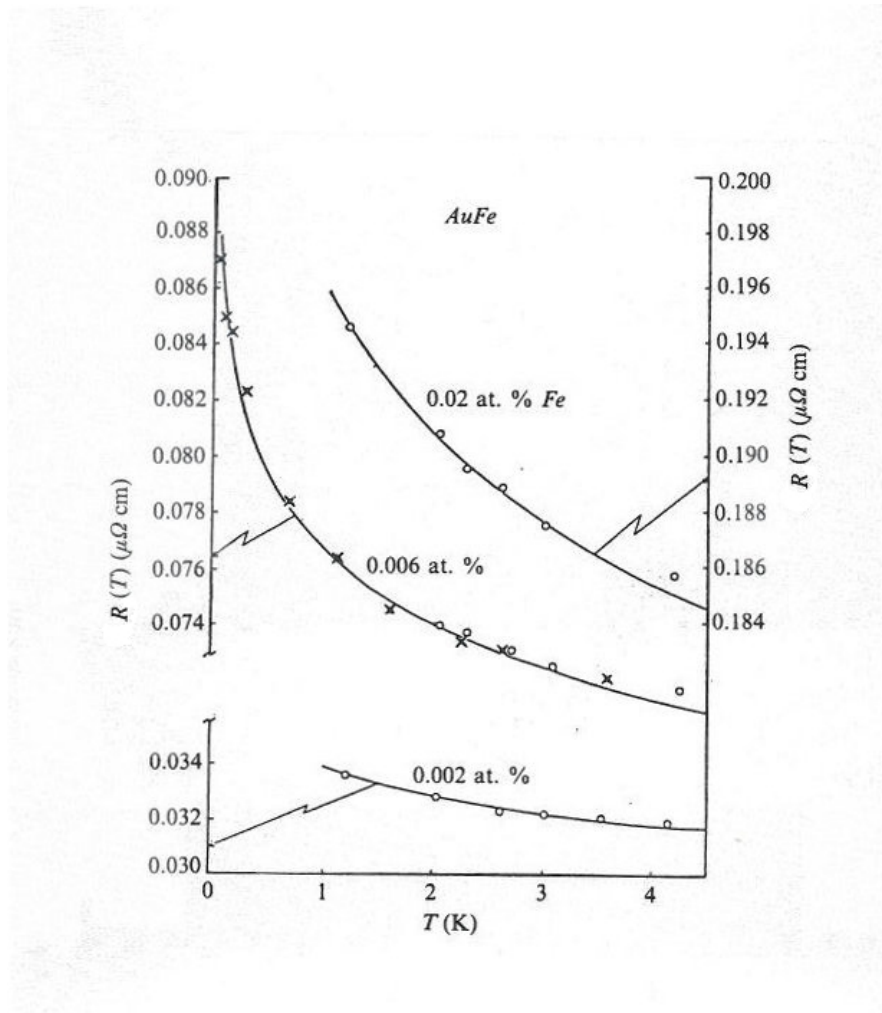


FIGURE 1.2: Figure from Kondo's original paper in 1964 [11], showing the agreement in resistance between experimental results (points) and the expected values using Kondo's model, for gold with different densities of iron impurities.

the logarithmic behavior from experimental results. [12] This reason is easier to understand in another model for a magnetic impurity inside a conducting metal, namely the Anderson model [13].

1.1.1 The Anderson model

The Anderson model describes a magnetic impurity as a single electron level ϵ_f accompanied by an on-site interaction U (which, if positive, reduces the probability of double occupancy). The electron level interacts with the conduction electrons through a hybridization parameter V . For a tight-binding Hamiltonian (similar to the one used in

this project) the Anderson model can be written as

$$\begin{aligned}
 H_A = & - \sum_{\langle i,j \rangle, \sigma} t_{i,j} \left(c_{i,\sigma}^\dagger c_{j,\sigma} + h.c. \right) + V \sum_{\sigma} \left(c_{k,\sigma}^\dagger f_{\sigma} + h.c. \right) \\
 & + U f_{\uparrow}^\dagger f_{\downarrow}^\dagger f_{\downarrow} f_{\uparrow} + \epsilon_f \sum_{\sigma} f_{\sigma}^\dagger f_{\sigma},
 \end{aligned} \tag{1.2}$$

with c_i^\dagger (c_i) being the creation (annihilation) operator of a conduction electron at site i , and f^\dagger (f) being the creation (annihilation) operator of an electron at the impurity site. In this case, the Anderson impurity only interacts with conduction electrons at site k , but it can, in a more general description, also interact with electrons at other sites. To imitate the behavior of a magnetic orbital, the on-site energy ϵ_f is below the Fermi level E_F and the on-site interaction U is such that $\epsilon_f + U > E_F$. This configuration ensures that the impurity site is occupied and at the same time resists double occupation, giving the site a magnetic moment.

In the situation of $\epsilon_f < E_F$ and $\epsilon_f + U > E_F$ with a single electron occupying the impurity site, it is classically forbidden for the electron to escape the impurity, or for another electron to enter the impurity site, as these processes violate the conservation of energy. In quantum mechanics however, this violation is permitted as long as the total energy of the system is restored within the time frame allowed by the uncertainty principle. This allows for two spin flip processes:

1. The electron in the impurity tunnels out of the impurity and an electron of opposite spin enters.
2. An electron of opposite spin tunnels into the impurity and the first electron leaves.

The electron at the impurity site is, through these two processes, able to share its potential with electrons around it. The first process is completely blind to spin because an electron of the same spin is as likely to enter the impurity while it is empty as an electron of opposite spin. The second process however, is only possible for electrons of opposite spins due to the Pauli principle, and this is what causes the anti-ferromagnetic coupling that Kondo used in his calculations. A more explicit derivation of the anti-ferromagnetic coupling can be seen in the Schrieffer-Wolff transformation [14], where it is shown that the Anderson model for highly localized spins is equivalent to the Kondo model with anti-ferromagnetic spin coupling.

The spin-flip processes of the impurity atoms creates a sharp peak in the density of states at the Fermi energy, called the Kondo resonance. Scattering against the states of the Kondo resonance is what causes the temperature dependence in the resistance seen

in experiments. This is because the conduction electrons are, at low temperatures, closer to the Fermi energy and consequently also closer to the resonance levels. This means that the scattering probability increases, and thereby also the resistance. However, the logarithmic dependence of temperature Kondo found in his calculations makes the faulty prediction that the resistance will become infinite as $T \rightarrow 0$. The temperature at which Kondo's perturbation theory calculation breaks down is called the Kondo temperature, T_K :

$$k_B T_K = D \exp\left(-\frac{1}{2J\rho_0}\right), \quad (1.3)$$

with D being the width of the band and ρ_0 the density of states at the Fermi level.

The task to solve the temperature dependence of resistance for $T < T_K$ became known as the Kondo problem and it became a popular subject for theoreticians in the 60's and 70's. The conclusion was made that, at low temperatures, the magnetic moments of impurities would be increasingly screened by close-by electrons (Kondo screening) causing a saturation of the resistance as $T \rightarrow 0$. At $T = 0$ the impurity electrons would be completely screened and together with the surrounding electrons form a singlet state, a Kondo singlet. This picture was confirmed in 1975 by Wilson [15], who used a numerical renormalization group method to prove that the groundstate of the Kondo system in fact is a singlet. Later studies provided further insight into the problem, for example, Nozieres showed in a paper from 1974 [16] that at $T \ll T_K$ the electrons could be treated as a Fermi liquid using Landau Fermi liquid theory. Substantial progress has also been made on the experimental side, and today experimentalist are, for example, able to tune the Kondo effect in artificial atoms (i.e. quantum dots) by altering on-site energy and gate voltage of the dots [17]. The precursor behavior to the Kondo effect has also been studied experimentally in few electron quantum rings, [18] which is the kind of system considered in this thesis.

1.2 Quantum rings

The controlled manufacturing of nanorings has seen a vast progress during the last decades, and experimentalists are today able to create nanorings containing only a few electrons [19]. The ring topology allows interesting interactions with magnetic fields, and the Aharonov Bohm effect [20] has, for instance, been observed experimentally in quantum rings [21]. Furthermore, a recent study in the field of ultra-cold atoms by Jimenez-Garcia et al., shows how Peierls substitution (see 1.2.1) can be realized on optical engineered lattices [22]. This study, along with many others, has made quantum rings a popular system in which one can investigate core aspects of quantum mechanics

experimentally. The theoretical interest in ring systems has increased with the experimental advances and much of the theoretical work with nanorings is concerning rings pierced by a magnetic field. Such fields are often chosen to be zero at the perimeter of the ring (i.e. Aharonov-Bohm flux). Small rings subjected to these kind of magnetic fields generate what is called persistent currents, which are currents that do not diminish even if the ring contains impurities that in general would scatter the electrons.

1.2.1 Peierls substitution

The reason why a ring electron can feel a magnetic field piercing the ring without actually being in the field, is because the vector potential \vec{A} is non-zero. The Hamiltonian of an electron in a magnetic field directly depends on \vec{A} , that is,

$$H_{mag} = \frac{(\vec{p} + e\vec{A})^2}{2m_e} + g_e\mu_B\vec{S} \cdot \vec{B}. \quad (1.4)$$

The last term accounts for the Zeeman effect, which for an Aharonov-Bohm flux is 0. The substitution $\vec{p} \mapsto \vec{p} + e\vec{A}$ works well for the continuous limit, but the inclusion into a tight binding Hamiltonian, which is done through Peierls substitution requires further considerations.

For simplicity, let's consider the case of one electron in a constant vector potential \vec{A} . The canonical momentum operator, $\vec{p} + e\vec{A}$, can then be rewritten using the unitary transformation

$$\vec{p} + e\vec{A} = \exp(-ie\vec{A} \cdot \vec{r}/\hbar) \vec{p} \exp(ie\vec{A} \cdot \vec{r}/\hbar). \quad (1.5)$$

For a tight binding Hamiltonian

$$H_t = -t \sum_{\langle i,j \rangle} (c_i^\dagger c_j + h.c.) + \sum_i \epsilon_i c_i^\dagger c_i, \quad (1.6)$$

the vector field can be introduced using the same transformation:

$$\widetilde{H}_t = \exp(-ie\vec{A} \cdot \vec{r}/\hbar) H_t \exp(ie\vec{A} \cdot \vec{r}/\hbar). \quad (1.7)$$

The matrix elements in the site basis then becomes

$$\langle i | \widetilde{H}_t | j \rangle = \begin{cases} \exp(-ie\vec{A} \cdot \vec{r}_i/\hbar) \epsilon_i \exp(ie\vec{A} \cdot \vec{r}_j/\hbar) = \epsilon_i & \text{if } i = j \\ -t \exp(-ie\vec{A} \cdot \vec{r}_i/\hbar) \exp(ie\vec{A} \cdot \vec{r}_j/\hbar) = \\ -t \exp(ie\vec{A} \cdot (\vec{r}_j - \vec{r}_i)/\hbar) & \text{if } i = j \pm 1. \end{cases} \quad (1.8)$$

In the case of a non-constant vector potential $\vec{A}(\vec{r})$ the off-diagonal matrix elements connecting adjacent sites are given by

$$\langle i+1 | \widetilde{H}_t | i \rangle = -t \exp \left(ie/\hbar \int_{r_i}^{r_{i+1}} \vec{A}(\vec{r}) \cdot d\vec{r} \right). \quad (1.9)$$

A magnetic field piercing a ring in the z -direction such that it is zero at the perimeter of the ring, can be modeled by the following vector potential (in cylindrical coordinates) [23]:

$$\vec{A} = (A_r, A_z, A_\varphi), \quad A_r = A_z = 0, \quad A_\varphi = \begin{cases} \frac{B_0 r}{2} & \text{if } r \leq r_c \\ \frac{B_0 r_c^2}{2r} = \frac{\phi}{2\pi r} & \text{if } r > r_c, \end{cases} \quad (1.10)$$

which gives a total flux $\phi = \pi r_c B_0$ penetrating the ring. An electron moving a full circle around the magnetic field, in the positive direction, at the perimeter would hence acquire the following phase,

$$C_{2\pi} = \exp \left(i r_c \cdot e/\hbar \int_0^{2\pi} A_\varphi \cdot d\varphi \right) = \exp(i\phi \cdot e/\hbar) = \exp(i2\pi\phi/\phi_0), \quad (1.11)$$

where $\phi_0 = h/e$ is the flux quantum. In a ring with L equally-spaced sites at the perimeter of the ring an electron hopping between neighboring sites would acquire the phase $C = \exp(i2\pi\phi/(\phi_0 \cdot L))$ in the positive direction and C^* in the negative direction.

1.2.2 Quantum rings in the periodic Anderson model

Nanorings with dense magnetic impurities display intriguing spin properties as the Kondo effect and other spin-interactions can compete. Important features of such systems are, for example, highlighted by the Doniach phase diagram [24] which displays the competition between the formation of Kondo singlets and Ruderman-Kittler-Kasuya-Yoshida (RKKY) spin ordering [25–27]. RKKY spin ordering is, in short, an ordering of separate magnetic moments due to interaction through indirect exchange of conduction electrons. Although RKKY interaction is a more general concept, referring to any magnetic moments (e.g. the magnetic moments of nuclei), here in this thesis, it only refers to the magnetic impurities of the Anderson model.

A relevant model for studying nanostructures with dense magnetic impurities is the Periodic Anderson Model (PAM), in which all of the conduction sites are connected to one Anderson impurity site each. The PAM has been studied extensively in connection to heavy fermion physics, non-Fermi liquid behavior, etc. [28][29]. In this thesis we consider a quantum ring, consisting of six sites, in the PAM. Groundstate aspects of this system

have been investigated in previous work [6–8], but to the best of our knowledge, nothing has been done on the dynamical side. The main focus is to study how the system is affected by a magnetic field piercing the ring. The effect of local Zeeman interaction is, however, also investigated. We make the assumption that the impurity sites are located such that the hopping path from and to the impurities are perpendicular to the vector potential of the magnetic field. This means that the electrons hopping to and from the impurity sites do not acquire any phase factor, even for non-zero magnetic fields. Peierls substitution is thus only needed for the hopping terms in the conduction band, and the system Hamiltonian can be written as

$$\begin{aligned} \mathbb{H}(\tau) = & -t \sum_{i,\sigma} \left(c_{i,\sigma}^\dagger c_{i+1,\sigma} e^{i\tilde{\phi}(\tau)} + h.c. \right) + V \sum_{i,\sigma} \left(c_{i,\sigma}^\dagger f_{i,\sigma} + h.c. \right) \\ & + U \sum_i f_{i,\uparrow}^\dagger f_{i,\downarrow}^\dagger f_{i,\downarrow} f_{i,\uparrow} + \epsilon_f \sum_{i,\sigma} f_{i,\sigma}^\dagger f_{i,\sigma} \\ & \tilde{\phi}(\tau) = \frac{2\pi\phi(\tau)}{\phi_0 L}. \end{aligned} \quad (1.12)$$

Here $c_{i,\sigma}^\dagger$ ($c_{i,\sigma}$) refers to the creation (annihilation) of an electron of spin σ at the conduction site i , and $f_{i,\sigma}^\dagger$ ($f_{i,\sigma}$) refers to the creation (annihilation) of an electron of spin σ at the impurity site i . For most parts of the thesis, t is used as the unit of energy and is therefore kept at 1. For the cases of $t \neq 1$, another energy unit (t_0) will be used. Furthermore, the on-site interaction for the impurity sites is always chosen $U = 6$ and $\epsilon_f = -U/2 = 3$ which implies particle-hole symmetry. The hybridization parameter V is varied in the range $(0, 1.5]$. For some calculations we also add a local Zeeman term (H_Z) for a specific site (k) to the Hamiltonian, for a B -field that is always assumed to be zero in the x and y directions, to one of the conduction sites,

$$H_Z(\tau) = g\mu_B B_z(\tau) S_z \quad (1.13)$$

The Schrödinger equation is solved numerically for this Hamiltonian using Exact Diagonalization.

1.3 Computational considerations

A large part of the thesis project consisted of building a program utilizing the Exact Diagonalization (ED) technique, a numerical method used to solve eigenvalue problems $Ax = \lambda x$. This method is useful for the stationary eigenvalue Schrödinger equation

$$\mathbb{H}\psi_n = E_n\psi_n. \quad (1.14)$$

in a finite-basis situation (for example, to find the groundstate). The technique can also be utilized for solving the time-dependent Schrödinger equation (see Section 2.3 in the Methods chapter), but then the procedure is not as straightforward. The advantages of the ED lies in the versatility of the technique (i.e., it can be used for a variety of systems), as well as the fact that it is exact and only carries the approximations inherent in the model. These traits make it very useful as a benchmark for approximative methods. However, ED is not very useful for large systems as it is computationally very expensive. If we, for example, consider the case of an Ising chain where every electron site has two possible configurations $|\uparrow\rangle$ and $|\downarrow\rangle$, such a system would have a Hilbert space dimension of 2^n with n being the number of sites in the chain. A chain of just 40 sites would already have more than 1 trillion basis states, which is way beyond what is possible to handle computationally.

For one-dimensional systems, such as the the Ising chain, there exists however another exact technique called Density Matrix Renormalization Group (DMRG), which was used in this thesis as a test of the ED program for 1D systems. DMRG was introduced by White in 1992 [30, 31] and has since become a very popular method in the field of condensed matter physics. The idea behind DMRG is similar to the renormalization group (RG) which Wilson used for the Kondo problem. Several extensions to the DMRG method have been made, for instance, the extensions to two dimensions [32], and time-evolution procedures for the 1D case (t-DMRG). [33–35]

A time-evolution DMRG program (source code from [9]) was interfaced in python for easy use in Hubbard/Anderson type of systems, and then used in this thesis for testing the ED program. Since the method of t-DMRG is complicated and because the program was mainly used as a blackbox for calculations, no in-depth explanation will be provided here. Instead, in the result chapter (3), we will briefly discuss how DMRG results depend on a proper choice of the parameters. Furthermore, in a different, larger-scale project the DMRG code was used to benchmark a novel method which combines adiabatic local exchange-correlations potentials from time dependent density functional theory with the Second-Born non-equilibrium Green's function self-energy in a protocol aimed to avoid double-counting of interactions.

Chapter 2

Method

This chapter will explain the main aspects of the computer program that was built as part of the thesis, and used to produce most of the results (chap. 3). The different parts will be explained in the same order as they are executed in the program: firstly, the initialization of the calculation (i.e. the choice of basis, assembly of the Hamiltonian, groundstate calculation etc.), then the time evolution procedure, followed by calculation of expectation values and lastly post processing of results.

The program is written in Python and is built as an extension to an existing quantum computing module for Python, called Quantum Toolbox in Python (QuTiP). The QuTiP package provides classes for handling quantum objects such as state vectors and operators, a handful of solvers for time dependent calculations as well as many other features (see Fig. 2.1). It uses the modules Numpy and Scipy as a base, which means that all of the heavier calculations, such as matrix multiplication, diagonalization etc., are actually run in compiled Fortran- and C-code. Furthermore, the fact that QuTiP uses the very popular Numpy and Scipy packages makes it simple to write extensions for anyone with experience in scientific Python. Although QuTiP has worked as a framework for the program, it is mostly used for the more simple routines, such as calculating expectation values, whereas the main features (including the initialization of the problem and the time evolution routine) are essentially independent of QuTiP. Nevertheless, working within the QuTiP framework provides a good overall structure to the program and it makes the inclusion of more QuTiP features simple. The inclusion of such extra features (e.g. quantum optimal control theory) is, however, beyond the scope of this thesis.

The total number of basis states, i.e. the Hilbert space dimension, only depends on these parameters and can be expressed as

$$\dim \mathcal{H} = \dim \mathcal{H}_\uparrow \cdot \dim \mathcal{H}_\downarrow = \binom{N}{n_\uparrow} \cdot \binom{N}{n_\downarrow}. \quad (2.2)$$

In fact, it is also true that

$$\mathcal{H} = \mathcal{H}_\uparrow \times \mathcal{H}_\downarrow, \quad (2.3)$$

which is how the basis set is assembled in the program. This saves computational time, especially when $n_\uparrow = n_\downarrow$ since then the total basis is equal the spin up basis times itself. With the basis set known it is possible to construct the Hamiltonian.

At a specific time, the Hamiltonian is always represented by a complex Hermitian matrix, but since the Hamiltonian in general is time dependent, it is stored differently. The most general form of the Hamiltonian, that the program can handle, is

$$\mathbb{H}(t) = \sum_{\langle i,j \rangle, \sigma} (C_{i,j,\sigma}(t) c_{i,\sigma}^\dagger c_{j,\sigma} + h.c.) + \sum_i C_i(t) n_{i,\sigma} n_{i,\sigma'} + \sum_{i,\sigma} C_{i,\sigma}(t) n_{i,\sigma}, \quad (2.4)$$

but can in general be re-expressed as

$$\mathbb{H}(t) = \sum_i^n f_i(t) \cdot \mathbb{H}_i, \quad (2.5)$$

with n being a small number usually well below 10. Because of this, the Hamiltonian is stored as a list of tuples, each containing a matrix of the same dimensionality as the whole Hamiltonian (\mathbb{H}_i), together with a weight function ($f_i(t)$), and instead of rebuilding the whole Hamiltonian at every time-step, the different parts of the Hamiltonian are multiplied with their respective weight function and then summed (as in eq. 2.5). To save computation time, the Hamiltonian is re-evaluated only if any of the weight functions have changed.

All of the matrices are stored in sparse format, which means only the non-zero elements of the matrix are stored. If all the elements in a $1\text{M} \times 1\text{M}$ matrix were stored as double precision floats, it would sum up to $8 \cdot 10^{12} \text{Bytes} = 8\text{TB}$ which is about as large as the biggest commercially available hard drives on the market (2015). A typical sparse matrix of the same dimension for the systems considered in this thesis would instead only take up about 1GB, which means that it can be stored in the much faster working memory. Sparse matrix storage also has a great advantage when it comes to computation, which is that the zero parts of the matrix never need to be considered when performing for instance a matrix-multiplication.

2.2 Groundstate calculation

If no initial state is set by the user, the program will assume that the system is in its groundstate at $t = 0$, which means that $H(0)$ needs to be diagonalized. The eigenvector corresponding to the lowest eigenvalue is the groundstate which is then set as the seed state for the time evolution procedure. If the groundstate is degenerate it can be a bit tricky to choose which linear combination of the lowest eigenstates to use as seed state for the time evolution, but the concept of groundstate calculation is pretty much straightforward. However, even with a non-degenerate groundstate, performing a full or as in most cases partial diagonalization on a large matrix, remains a formidable task.

The program uses three different methods for calculating the groundstate. The first one is a full diagonalization of the system, this is only used for systems with $n < 3000$. The two other methods are both iterative, one is the implicitly restarted Lanczos method originally from ARPACK but wrapped for python in the Scipy module, the other one is the Jacobi-Davidson method from another Python module called Pysparse. In most cases Jacobi-Davidson performs better, but it has the downside that it only works (in the current implementation of Pysparse) for real symmetric matrices, while the Lanczos method works for Hermitian matrices as well. There are plans of implementing yet another routine for groundstate calculation that uses the Jacobi-conjugate preconditioned gradients method which is expected to perform better than the Lanczos method for Hermitian matrices when the eigenvalues are close to each other.

2.3 Time evolution

The time evolution of the system is calculated through solving the time-dependent Schrödinger equation,

$$i\hbar \frac{\partial |\psi(t)\rangle}{\partial t} = H(t) |\psi(t)\rangle. \quad (2.6)$$

By discretizing the time and assuming that the Hamiltonian is constant within each time-step the general solution of the Schrödinger equation can be expressed as

$$|\psi(t + \Delta t)\rangle = e^{-iH(t)\Delta t} |\psi(t)\rangle, \quad 0 \leq \Delta t \leq ht \quad (2.7)$$

with ht being the time-step. By substituting $H(t)$ with $Z(t)D(t)Z^\dagger(t)$ we get the expression

$$\begin{aligned} |\psi(t + \Delta t)\rangle &= e^{-iZ(t)D(t)Z^\dagger(t)\Delta t} |\psi(t)\rangle \\ &= Z(t)e^{-iD(t)\Delta t}Z^\dagger(t) \cdot |\psi(t)\rangle, \end{aligned} \quad (2.8)$$

which can be evaluated numerically, but with the downside that it requires a full diagonalization at every time-step. This is not an option for large matrices. However, it turns out that, as in the case of the groundstate calculation only a partial diagonalization is needed.

The method for time evolution used in the program is called Lanczos-adapted time evolution [37], and it uses the Lanczos algorithm to find a small subspace in which the Hamiltonian is diagonalized. It is an iterative method that, through repeated multiplication of the Hamiltonian with the state vector $|\psi(t)\rangle$ and together with an orthogonalization procedure expresses the Hamiltonian as a tridiagonal matrix within a subspace around $|\psi(t)\rangle$. By exactly diagonalizing the Hamiltonian matrix within a small subspace of the Hilbert space, computational time is significantly reduced with hardly any loss of accuracy.

Lanczos time evolution uses the fact that the state vector $|\psi(t + \Delta t)\rangle$ movement in the Hilbert space is confined within a specific subspace for small values of Δt (illustrated in Fig. 2.2). This space is called the Krylov subspace and, for $|\psi(t)\rangle$ and iteration order r , is expressed as:

$$\mathcal{K}_r(\mathbb{H}, |\psi(t)\rangle) = \text{span}\{|\psi(t)\rangle, \mathbb{H}|\psi(t)\rangle, \mathbb{H}^2|\psi(t)\rangle, \dots, \mathbb{H}^{r-1}|\psi(t)\rangle\}. \quad (2.9)$$

By comparing the right hand side of eq. 2.9 to the Schrödinger equation (eq. 2.6) we see that $\mathcal{K}_r(\mathbb{H}, |\psi(t_0)\rangle)$ is actually the space spanned by the time derivatives of $|\psi(t_0)\rangle$ up to order $r - 1$. The typical value of r used in the time evolution algorithm is 10 but can be adjusted depending on situation, e.g. if the Hamiltonian changes very slowly, a larger time-step can be used and this can be compensated by a larger order of the Krylov space or vice versa.

For the Hamiltonian to be diagonalized within the Krylov subspace, a basis has to be chosen. The first choice that may come to mind is the vectors in the right hand side of eq. 2.9, but for several numerical reasons it is better to find another basis. For instance, there is no guarantee that the $\mathbb{H}^i|\psi(t_0)\rangle$ vectors are unique; it may very well be that $|\psi(t_0)\rangle$ is actually an eigenstate of \hat{H} in which case all of the vectors are the same. The set of basis vectors for the Krylov subspace used in the computer program made in this thesis are the Lanczos vectors, which are orthonormal.

To find the Lanczos vectors one starts with a seed state which can be chosen arbitrarily, and this is the first of the Lanczos vectors. For the time evolution procedure this vector is the current state vector. $|\psi(t)\rangle = |Q_1\rangle$. By applying the Hamiltonian to this vector we get another vector $|v\rangle$, which can be described as a linear combination of the first

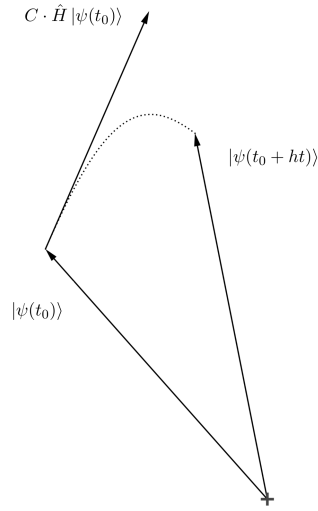


FIGURE 2.2: Illustrative picture of the state movement in the Hilbert space.

and the second Lanczos vectors.

$$\mathbf{H} |Q_1\rangle = |v\rangle = \alpha_1 |Q_1\rangle + \beta_2 |Q_2\rangle \quad (2.10)$$

The value of α_1 can be found by performing the scalar product $\langle Q_1 | \mathbf{H} |v\rangle$ and $\beta_2 |Q_2\rangle$ is simply $|v\rangle - \alpha_1 |Q_1\rangle$. It is also worth noting that

$$\beta_2 = \langle Q_2 | v \rangle = \langle Q_2 | \mathbf{H} |Q_1\rangle. \quad (2.11)$$

By multiplying the Hamiltonian with the newest Lanczos vector $|Q_2\rangle$ we get yet another vector $|w\rangle$ which can be written as a linear combination of a vector in the $(|Q_1\rangle, |Q_2\rangle)$ plane as well as a vector $|Q_3\rangle$ (the third Lanczos vector) perpendicular to $(|Q_1\rangle, |Q_2\rangle)$,

$$\mathbf{H} |Q_2\rangle = |w\rangle = \gamma |Q_1\rangle + \alpha_2 |Q_2\rangle + \beta_3 |Q_3\rangle, \quad (2.12)$$

and by taking the scalar products $\langle Q_i | w \rangle, i = 1, 2, 3$ we get

$$\langle Q_1 | \mathbf{H} |Q_2\rangle = \gamma, \quad \langle Q_2 | \mathbf{H} |Q_2\rangle = \alpha_2, \quad \langle Q_3 | \mathbf{H} |Q_2\rangle = \beta_3. \quad (2.13)$$

Moreover, through comparison with eq. 2.11, and due to the hermicity of the Hamiltonian operator, we also get that $\gamma = \beta_2$.

In the next step of the procedure we get

$$\mathbf{H} |Q_3\rangle = |s\rangle = \delta |Q_1\rangle + \epsilon |Q_2\rangle + \alpha_3 |Q_3\rangle + \beta_3 |Q_4\rangle, \quad (2.14)$$

$$(2.15)$$

and if we now perform the scalar products $\langle Q_i | s \rangle$, $i = 1, 2, 3, 4$ we get

$$\begin{aligned} \langle Q_1 | H | Q_3 \rangle &= (\alpha_1 \langle Q_1 | + \beta_2 \langle Q_2 |) | Q_3 \rangle = 0, & \langle Q_2 | H | Q_3 \rangle &= \epsilon = \beta_3. \\ \langle Q_3 | H | Q_3 \rangle &= \alpha_3, & \langle Q_4 | H | Q_3 \rangle &= \beta_4 \end{aligned} \quad (2.16)$$

In fact, $\langle Q_i | H | Q_j \rangle = 0$ for all $i - j \geq 2$, and by continuing the procedure we get

$$\langle Q_i | H | Q_i \rangle = \alpha_i, \quad \langle Q_i | H | Q_{i+1} \rangle = \langle Q_{i+1} | H | Q_i \rangle = \beta_{i+1}, \quad (2.17)$$

which means that we can express the Hamiltonian matrix in the basis of the Lanczos vectors:

$$\langle Q_i | H | Q_j \rangle = \tilde{H} \hat{=} \begin{bmatrix} \alpha_1 & \beta_2 & 0 & 0 & \cdots \\ \beta_2 & \alpha_2 & \beta_3 & 0 & \cdots \\ 0 & \beta_3 & \alpha_3 & \beta_4 & \cdots \\ 0 & 0 & \beta_4 & \alpha_4 & \cdots \\ \vdots & \vdots & \vdots & \vdots & \ddots \end{bmatrix}. \quad (2.18)$$

If $|Q_1\rangle$ would be an eigenvector of the Hamiltonian, then all the elements of eq. 2.18 would be zero except α_1 which would have the eigenvalue corresponding to $|Q_1\rangle$, which is perfectly fine when treating everything analytic. However, when numerically treating these vectors we only have a finite accuracy and if any $|Q_i\rangle$ happen to be close to an eigenvector of the Hamiltonian then we have that

$$H |Q_i\rangle \approx \alpha_i |Q_i\rangle + \beta_{i+1} |Q_{i+1}\rangle, \quad \beta_{i+1} \sim 0. \quad (2.19)$$

Hence, if β_{i+1} is a very small quantity, then the subtraction $\beta_{i+1} |Q_{i+1}\rangle = H |Q_i\rangle - \alpha_i |Q_i\rangle$ becomes a very numerical unstable process, which means the resulting vector $|Q_{i+1}\rangle$ can end up anywhere in the Hilbert space. This is avoided by adding a stopping condition to the Lanczos iteration, i.e. if $\beta_i < \beta_{min}$ then the procedure is stopped. The typical stopping value used is $\beta_{min} = 10^{-12}$ and if the condition $\beta_i < \beta_{min}$ is not reached, then the procedure is stopped when the maximum order of the Krylov space is reached.

Eq. 2.8 is solved within the Krylov subspace by just performing a simple basis change from the regular basis vectors (eq. 2.1) to the Lanczos vectors, and following the procedure of 2.8 within the subspace and then change the basis back the regular basis (eq. 2.1):

$$|\psi(t + \Delta t)\rangle = Q \tilde{Z}(t) e^{-i\tilde{D}(t)\Delta t} \tilde{Z}^\dagger(t) Q^\dagger |\psi(t)\rangle \quad (2.20)$$

with

$$Q = \begin{bmatrix} | & | & \cdots & | \\ Q_1 & Q_2 & \cdots & Q_{k_{max}} \\ | & | & \cdots & | \end{bmatrix}. \quad (2.21)$$

The Lanczos adapted time evolution dramatically increases the dimension of viable systems, easily up to a few million, without compromising with accuracy (given small enough time-step and large enough Krylov space dimension). As a final remark, in the time evolution the Hamiltonian is evaluated at time $t + \Delta t/2$ instead of t resulting in an extra order of accuracy with respect to Δt .

2.4 Operators

Although the state vector contains all of the information about the system it is by itself useless in most cases, especially in higher Hilbert space dimensions as it is then very hard to interpret. To make sense of all the information contained in the state vector we calculate expectation values for various operators for observables of interest. In the program the operators are all expressed in terms of sparse matrices and the routine which calculates the expectation value simply calculates

$$\langle \hat{O}(t) \rangle = \langle \psi(t) | \hat{O} | \psi(t) \rangle. \quad (2.22)$$

The operators \hat{O} can correspond to concrete observables like charge density, currents etc., but also to more abstract concepts like spin correlations and entanglement. When treating time dependent Hamiltonians it can be (as we will see in the case of the current operator) that the operator also is time dependent which may become a bit complicated numerically, but otherwise the procedure is straight forward.

2.4.1 Current

The current operator for the Hamiltonian in equation 1.12 can be derived from the continuity equation and the Heisenberg equation of motion,

$$\frac{\partial n_i}{\partial t} = i [H, n_i] = \nabla J = J_i - J_{i+1} - J_f, \quad (2.23)$$

with the direction of J_i , J_{i+1} , J_f defined as in Figure 2.3.

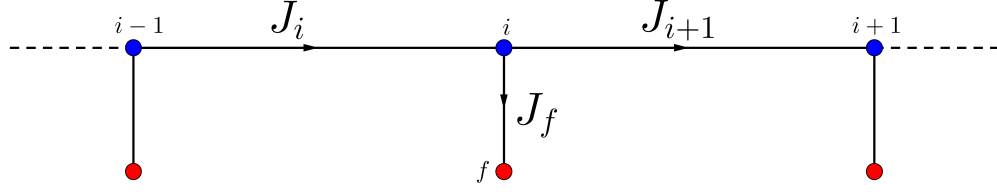


FIGURE 2.3: Currents affecting the electron density at site i . In this configurations the divergence of J at site i is $\nabla J = J_i - J_{i+1} - J_f$.

Most of the terms in the Hamiltonian commute with n_i and can be left out when performing the commutator between n and the Hamiltonian,

$$[\mathbb{H}, n_i] = \left[-t \left(c_{i+1}^\dagger c_i \cdot e^{i\phi} + c_i^\dagger c_{i+1} \cdot e^{-i\phi} + c_i^\dagger c_{i-1} \cdot e^{i\phi} + c_{i-1}^\dagger c_i \cdot e^{-i\phi} \right), n_i \right] + \left[V \left(c_i^\dagger c_f + c_f^\dagger c_i \right), n_i \right]. \quad (2.24)$$

Calculating the first part of eq. 2.24 gives,

$$\begin{aligned} & \left[-t \left(c_{i+1}^\dagger c_i \cdot e^{i\phi} + c_i^\dagger c_{i+1} \cdot e^{-i\phi} + c_i^\dagger c_{i-1} \cdot e^{i\phi} + c_{i-1}^\dagger c_i \cdot e^{-i\phi} \right), n_i \right] \\ &= -t \left((c_i^\dagger c_{i-1} \cdot e^{i\phi} - c_{i-1}^\dagger c_i \cdot e^{-i\phi}) - (c_{i+1}^\dagger c_i \cdot e^{i\phi} - c_i^\dagger c_{i+1} \cdot e^{-i\phi}) \right), \end{aligned} \quad (2.25)$$

where J_i and J_{i+1} can be identified as

$$J_i = -it \left(c_i^\dagger c_{i-1} \cdot e^{i\phi} - c_{i-1}^\dagger c_i \cdot e^{-i\phi} \right) = -2itc_i^\dagger c_{i-1} \cdot e^{i\phi}, \quad (2.26)$$

$$J_{i+1} = -it \left(c_{i+1}^\dagger c_i \cdot e^{i\phi} - c_i^\dagger c_{i+1} \cdot e^{-i\phi} \right) = -2itc_{i+1}^\dagger c_i \cdot e^{i\phi}. \quad (2.27)$$

The current operator J_f is found by calculating the second part of eq. 2.24 which yields

$$J_f = -2itf^\dagger c_i. \quad (2.28)$$

This operator is however never used in the code because for the system we consider, the information it provides can be accessed by simply taking the time derivative of $\langle n_f \rangle$. The currents J_i and J_f are density both currents. To get the charge current, which is the quantity used in the results, one has to multiply with the electron charge which is $-e = -1$.

2.4.2 Spin correlations

Spin-spin correlations are very useful observables to look at as they give a lot of information about the magnetic state of the system. The program has implemented two types of spin-spin correlation operators. One for the z -component of the spin, $\langle \psi(t) | S_z^{(i)} S_z^{(j)} | \psi(t) \rangle$, and the other one for the full S -vector, $\langle \psi(t) | S^{(i)} \cdot S^{(j)} | \psi(t) \rangle$. The z -component of the spin is easy to calculate as the system basis is expressed in the z -projection of the spin, which means that the z -component of the spin operator can be written as

$$S_z^{(i)} = \frac{1}{2} (n_{i,\uparrow} - n_{i,\downarrow}), \quad (2.29)$$

and the spin-spin correlation operator is simply

$$S_z^{(i)} S_z^{(j)} = \frac{1}{4} (n_{i,\uparrow} - n_{i,\downarrow}) (n_{j,\uparrow} - n_{j,\downarrow}) = \frac{1}{4} (n_{i,\uparrow} n_{j,\uparrow} + n_{i,\downarrow} n_{j,\downarrow} - n_{i,\uparrow} n_{j,\downarrow} - n_{i,\downarrow} n_{j,\uparrow}) \quad (2.30)$$

In the definition of spin-spin correlations used in the results the factor $\frac{1}{4}$ is removed. By removing this factor, we end up with a quantity that ranges from -1 to 1, with -1 corresponding to a perfect anti-ferromagnetic configuration, and 1 to a perfect ferromagnetic.

To define the total spin operator we make use of the spin ladder operators $S_+^{(i)}$ and $S_-^{(i)}$ which are defined as

$$\begin{cases} S_+^{(i)} &= S_x^{(i)} + i S_y^{(i)} \\ S_-^{(i)} &= S_x^{(i)} - i S_y^{(i)} \end{cases} \implies \begin{cases} S_x^{(i)} &= \frac{S_+^{(i)} + S_-^{(i)}}{2} \\ S_y^{(i)} &= \frac{S_+^{(i)} - S_-^{(i)}}{2i} \end{cases} \quad (2.31)$$

The total spin-spin correlation operator then becomes,

$$\begin{aligned} S^{(i)} S^{(j)} &= S_x^{(i)} S_x^{(j)} + S_y^{(i)} S_y^{(j)} + S_z^{(i)} S_z^{(j)} \\ &= \frac{1}{4} \left((S_+^{(i)} + S_-^{(i)}) (S_+^{(j)} + S_-^{(j)}) - (S_+^{(i)} - S_-^{(i)}) (S_+^{(j)} - S_-^{(j)}) \right) + S_z^{(i)} S_z^{(j)} \\ &= \frac{1}{2} \left(S_+^{(i)} S_-^{(j)} + S_-^{(i)} S_+^{(j)} \right) + S_z^{(i)} S_z^{(j)} \\ &= \frac{1}{2} \left(c_{i,\uparrow}^\dagger c_{i,\downarrow} c_{j,\downarrow}^\dagger c_{j,\uparrow} + c_{i,\downarrow}^\dagger c_{i,\uparrow} c_{j,\uparrow}^\dagger c_{j,\downarrow} \right) + S_z^{(i)} S_z^{(j)} \end{aligned} \quad (2.32)$$

At the last step we made use of the fact that $S_+^{(i)}$ and $S_-^{(i)}$ correspond to spin flips that can be expressed in electron creation and annihilation operators, e.g. $S_+^{(i)} = c_{i,\uparrow}^\dagger c_{i,\downarrow}$.

2.5 Entanglement and concurrence

Entanglement is one of the more perplexing consequences of quantum mechanics. The fact that the measurements made on one particle A can affect the state of another particle B is quite strange, to say the least. To understand the concept of entanglement better, one has to abandon the thought of two distinct objects and instead see them as one composite system. If, when considering all of the possible outcomes of this system, the probability of finding particle A in a specific state is dependent on the state of particle B, then the particles are entangled. This is just a conditional probability, which is very common even in the classical world.

A common approach to quantify entanglement is through concurrence, which is a measure of the entanglement of a two-qubit system. A qubit state is the quantum mechanical analog of a classical bit, and it can, instead of just being either 0 or 1, also be in a superposition state:

$$|\psi\rangle = \alpha|0\rangle + \beta|1\rangle. \quad (2.33)$$

In this thesis we consider a model in which every occupied site can be seen as a qubit spin state. To calculate the concurrence between two sites, the density matrix of the two spin qubit system is constructed using the basis $\{|\uparrow\uparrow\rangle, |\uparrow\downarrow\rangle, |\downarrow\uparrow\rangle, |\downarrow\downarrow\rangle\}$. Due to the choice of basis for the whole system (eq. 2.1), the total spin is conserved and the density matrix, for the sites i and j , in general becomes

$$\rho_{i,j} = \begin{bmatrix} a & 0 & 0 & 0 \\ 0 & b & c & 0 \\ 0 & c & \tilde{b} & 0 \\ 0 & 0 & 0 & \tilde{a} \end{bmatrix}, \quad (2.34)$$

with $a = \tilde{a}$ and $b = \tilde{b}$ for cases that are symmetric in respect to spin up and spin down electrons.

The concurrence of site i and j is given by

$$C_{i,j} = \max(0, \sqrt{\lambda_1} - \sqrt{\lambda_2} - \sqrt{\lambda_3} - \sqrt{\lambda_4}) \quad (2.35)$$

with $\lambda_1 > \lambda_2 > \lambda_3 > \lambda_4$ being the eigenvalues of the matrix $\rho_{i,j}\tilde{\rho}$ where

$$\tilde{\rho} = (\sigma_y \otimes \sigma_y)\rho_{i,j}(\sigma_y \otimes \sigma_y). \quad (2.36)$$

The maximum value of the concurrence $C = 1$ is reached for a singlet spin state,

$$\frac{1}{\sqrt{2}}(|\uparrow\downarrow\rangle - |\downarrow\uparrow\rangle). \quad (2.37)$$

Chapter 3

Results

This chapter presents the results of the thesis, and it is divided into three sections. The first section is concerned with the computational aspects of the work, and it contains a comparison between the exact diagonalization program developed in the thesis project, a t-DMRG program, two common many-body approximation (MBA) techniques (Second Born and BALDA), and a novel method we will denote as Hybrid, that combines the strengths of Second Born and BALDA. The section also includes a figure that explains the most important convergence parameters of the t-DMRG technique. In the second section, results for pure, 1D quantum rings are presented. The third section is concerned with quantum rings in the periodic Anderson model. It will be divided into two subsections: the first contains results on persistent currents in connection to spin-spin correlations and entropy, and the second subsection presents results for when the ring is disturbed by a local magnetic field at one of the conduction sites.

3.1 Comparison of computational techniques

The system considered in this section is a linear chain of eight sites at half filling, with four spin up electrons and four spin down electrons. The fifth site (from the left) is an Anderson impurity site with $U = 4$. The system can be seen as a miniature of two leads connected to a quantum dot, which is a common experimental setup as well as a popular system for theoretical studies. However, it should be emphasized that since this system consists of only eight sites, it is far from sufficient in size to draw any conclusions that extends to the behavior of larger systems. Nevertheless, the size of the system is sufficient for the purpose of comparison between different computational techniques.

The procedure for every technique is as follows: Firstly, the groundstate is calculated, then the system is disturbed by an external field and the time-evolution of the system is

calculated. We use two different perturbations that are common for lead-dot-lead setups. The first one is a sudden, asymmetric bias applied over the leads. In this case, it means that the onsite energies of the four leftmost sites are lifted. The second perturbation corresponds to a Gaussian pulse over the gate voltage, that is, the onsite energy of the impurity site. We compare the results of the different techniques looking at the electron density at the impurity site.

In figure 3.1 the electron density of the impurity site is shown after the system is disturbed by the asymmetric lead bias

$$V_{Bias} = 0.5\theta(\tau). \quad (3.1)$$

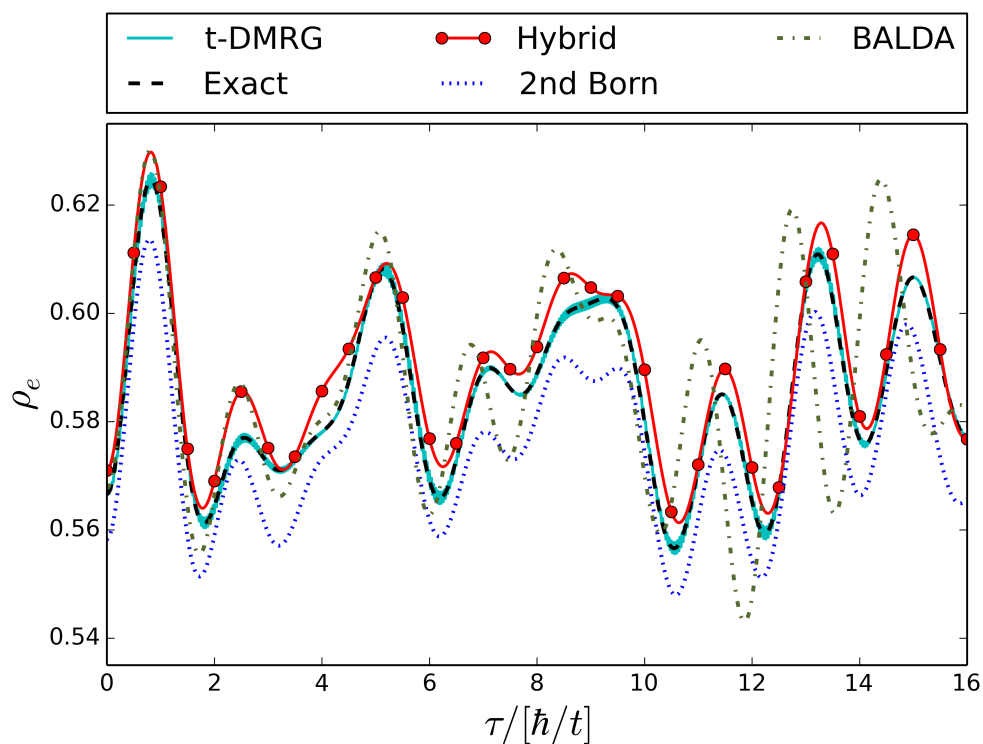


FIGURE 3.1: Electron density calculated with different computational techniques for an eight site tight binding chain with the fifth site (from the left) being an Anderson impurity site with $U = 4$. The system is perturbed by a step potential $V_{Bias} = 0.5\theta(\tau)$ on the four leftmost sites. The t-DMRG and Exact diagonalization results (cyan and dashed black line) display the exact solution.

It is clear in figure 3.1 that the electron density calculated with two exact techniques, t-DMRG and exact diagonalization, follow the same curve. Since two independent exact programs utilizing different techniques produce the same results, we conclude that this in fact is the exact result, and use these curves as benchmark for the the MBA techniques. Out of the MBA techniques it is clear that the Hybrid method performs better in this

setup. It is closer to the exact solution at most points, and it reproduces most of the characteristics seen in the exact curve. BALDA reproduces the exact results as well as the Hybrid in the beginning, but for longer times it becomes increasingly out of phase. Second Born on the other hand performs well when it comes to the phase, but it is systematically below the exact solution.

Figure 3.2 also displays the electron density at the impurity site, but this time for the second type of perturbation, that is, the on-site energy of the impurity atom is changed instead of adding a bias over the leads. The change in the gate voltage is a Gaussian pulse of the form

$$V_G = -\exp(-(\tau - 2.5)^2/0.4). \quad (3.2)$$

The exact methods are, as in figure 3.1, on top of each other and their common result is interpreted as the exact solution. BALDA reproduces much of the behavior of the exact solution at times $\tau < 6$, but it is again out of phase at larger times, whereas second Born and the Hybrid method perform much better. The Hybrid solution might be slightly better at reproducing characteristics of the exact curve, but it is, aside from that fact, hard to tell apart from the Second Born solution.

It should be noted that although the exact diagonalization technique is very effective in this arena, it fails at larger systems, and is therefore not an option for realistic investigations of lead-dot-lead systems.

In figure 3.3 we look at the same system and perturbation as we did in in figure 3.1. This time, instead of looking at the actual solution we look at how much the t-DMRG solution differs from the solution calculated in the exact diagonalization program depending on the size of the renormalization matrix in the DMRG procedure. We will not go into any detail on how this parameter really works in the DMRG method, and the interested reader is referred to "DMRG for dummies" [38], which is a review article on the subject. The size, m , of the renormalization matrix is related to the truncation of the total Hilbert space, and it is vital that any DMRG-calculation is checked on convergence in m .

To illustrate the dependence of m in t-DMRG calculations, we plot the running mean of the relative error for different values of m against time. The reason for using a running mean instead of directly plotting the relative errors is because, in this case, the different solutions frequently cross the exact solution which makes it harder to read and understand the figure.

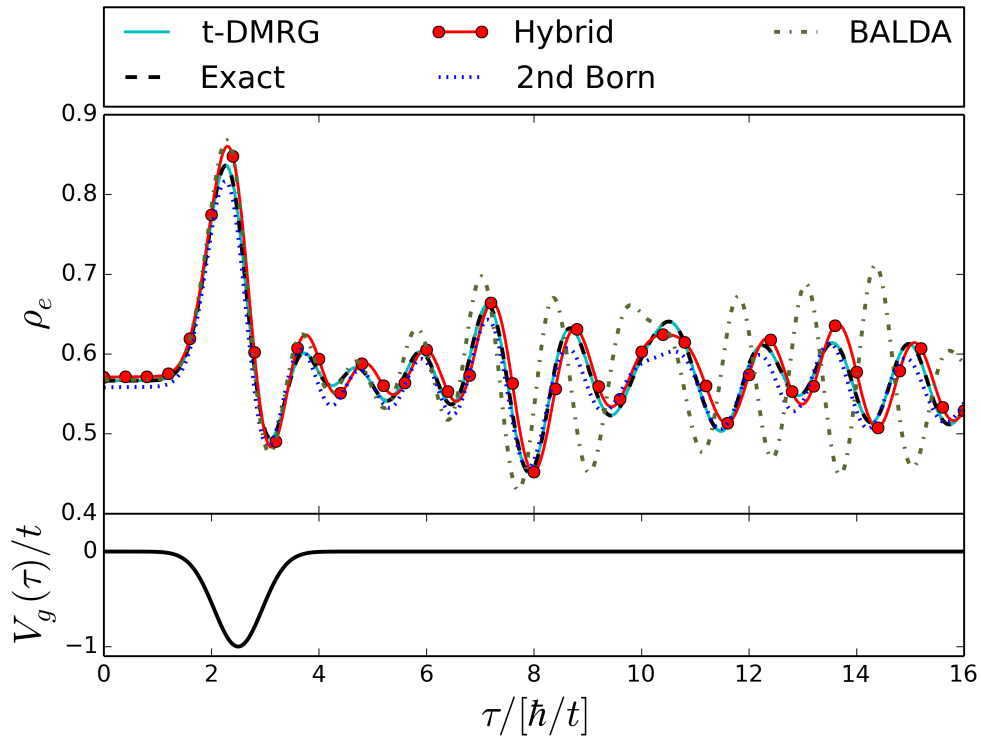


FIGURE 3.2: Electron density calculated with different computational techniques for an eight site tight binding chain with the fifth site (from the left) being an Anderson impurity site with $U = 4$. The system is perturbed by a Gaussian pulse, $V_G = -1 \exp(-(\tau - 2.5)^2/0.4)$, on the on-site energy of the impurity site. The t-DMRG and Exact diagonalization results (cyan and dashed black line) display the exact solution.

The running mean of the relative error is calculated using

$$M_x(\tau, T) = \frac{1}{T} \int_{\tau}^{\tau+T} \left| \frac{x(\tau') - x_0(\tau')}{x_0(\tau')} \right| d\tau', \quad (3.3)$$

with T being the time period in which the relative error is averaged ($T = 1$ in the fig 3.3).

It is clear in figure 3.3 that $m \leq 16$ is not sufficient even for an accurate calculation of either the groundstate, or the time evolution. For $m \geq 32$ things however become a bit more complicated, and $m = 32$ is, for example, high enough for the groundstate calculation to converge. However, for longer times, the $m = 32$ curve diverges from the correct solution. In this case the solution gradually diverges, but it is often the case that there is a time, called the runaway time, after which the accuracy drastically drops.

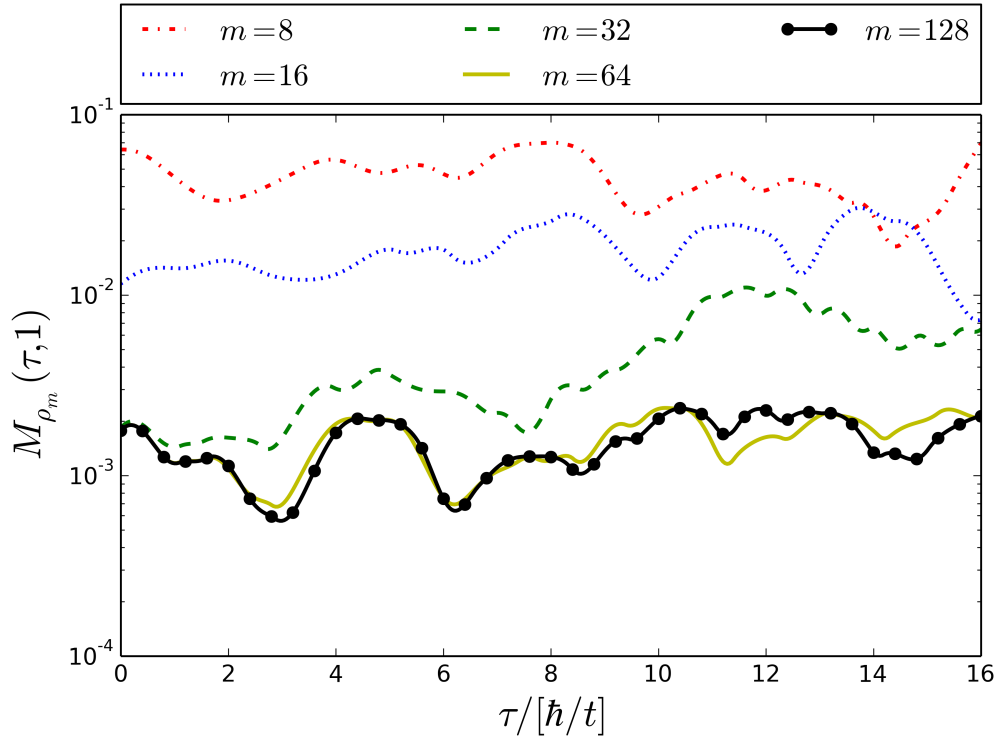


FIGURE 3.3: Running mean of relative error of the electron density calculated using t-DMRG, using different sizes of the renormalization matrix, m . The system considered is an eight site tight-binding chain, with the fifth site (from the left) being an Anderson impurity site with $U = 4$ and a gate voltage of $V_G = 0.25$. The system is perturbed by a step potential of the form $V_{bias}(\tau) = 0.5 \cdot \theta(\tau)$ on the four leftmost sites. The figure shows the running mean (calculated using eq. 3.3 with $T = 1$) of the relative error for calculations done using different m .

The runaway time depends on m , but also on the number of time steps the system has been evolved. The time at which the solution starts to diverge can therefore be pushed forward in time by either increasing m , or by increasing the time step. However, an increase of the time step introduces another error because of the time discretization which also needs to be taken into consideration. A more in-depth explanation of the runaway time can be found in [39]. For the cases of $m = 64$ and $m = 128$, the results are more or less converged, with respect to m , for the time frame of interest, but at longer times the $m = 64$ solution would likely diverge earlier. Larger systems require a larger m to converge, but the growth of m with respect to the size of the system is different for each system. In general one can say that for more strongly correlated systems the required value of m grows faster with respect to the system size.

3.2 One-dimensional quantum rings

This section presents results that highlight some important concepts in the area of one dimensional quantum rings without impurities. These results are not to be seen as original work, and they are included for the purpose of discussion in connection with the results for quantum rings in the PAM (section 3.3).

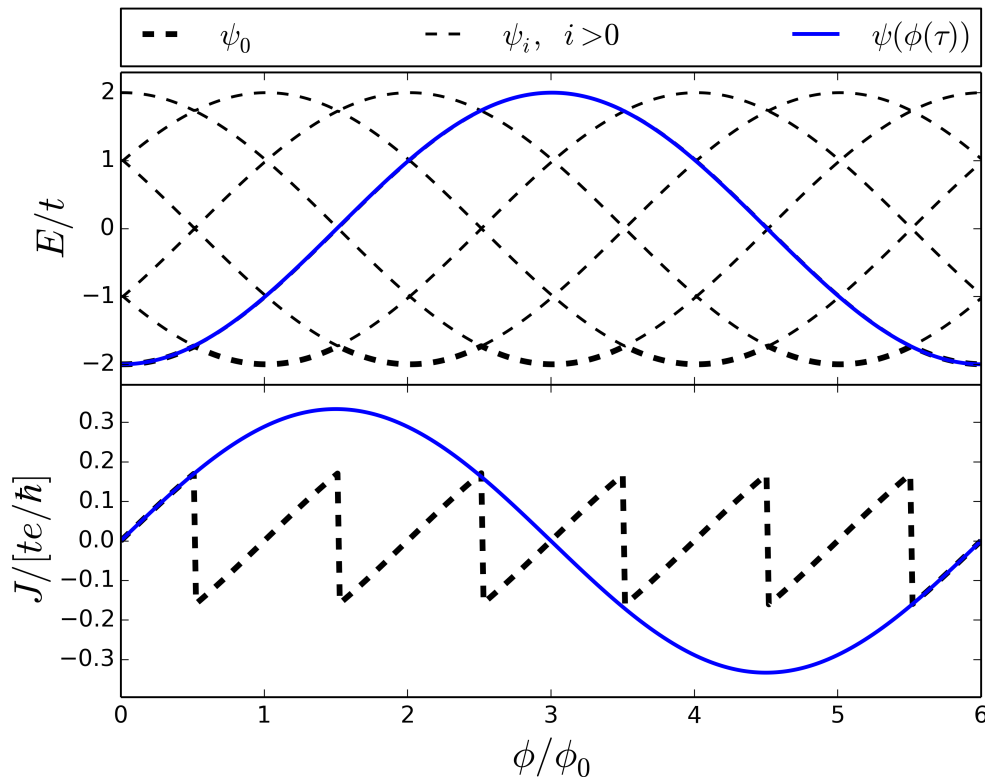


FIGURE 3.4: Steady state and time-evolution calculated energies and currents of a six site ring containing one electron. The state of the time-evolved system, $\psi(\phi(\tau))$, is independent of $\phi(\tau')$ for $\tau' < \tau$. $\phi(\tau)$ represents any ramping of the flux that is $\phi(\tau)$ at time τ . Note the difference in period of the current between the groundstate and time evolution calculations.

In figure 3.4 the simple case of one electron in a 1D quantum ring consisting of six sites, pierced by a magnetic field, is considered. The energy levels and persistent currents are shown as a function of the magnetic flux, as well as the energy and current for a system which is ramped from zero flux. Interestingly, even with adiabatic ramping, the system ends up in a different energy state than the groundstate for $0.5\phi_0 < \phi < 5.5\phi_0$. In fact, the state of the system is independent of how the flux is ramped. Furthermore, when the flux is ramped, the periodicity of the current changes from ϕ_0 , as is the case for the groundstate calculations, to $L\phi_0$, with L being the number of sites. It should be noted that $L\phi_0$ is exactly the periodicity of the Hamiltonian. Figure 3.4 only displays the case of one electron in the ring, but the same qualitative behavior is observed for the case

of more electrons in the ring, as long as the onsite interaction between the electrons is kept at zero.

Figure 3.5 displays results for the case of a quantum ring with six sites this time with an electron-electron onsite interaction of $U/t = 3$. The inclusion of the onsite interaction separates the groundstate of the system from the other states. Furthermore, as a contrast to figure 3.4, in this case the system remains in its groundstate for adiabatic ramping of the flux. However, in the case of non-adiabatic ramping, the system goes into higher excited states.

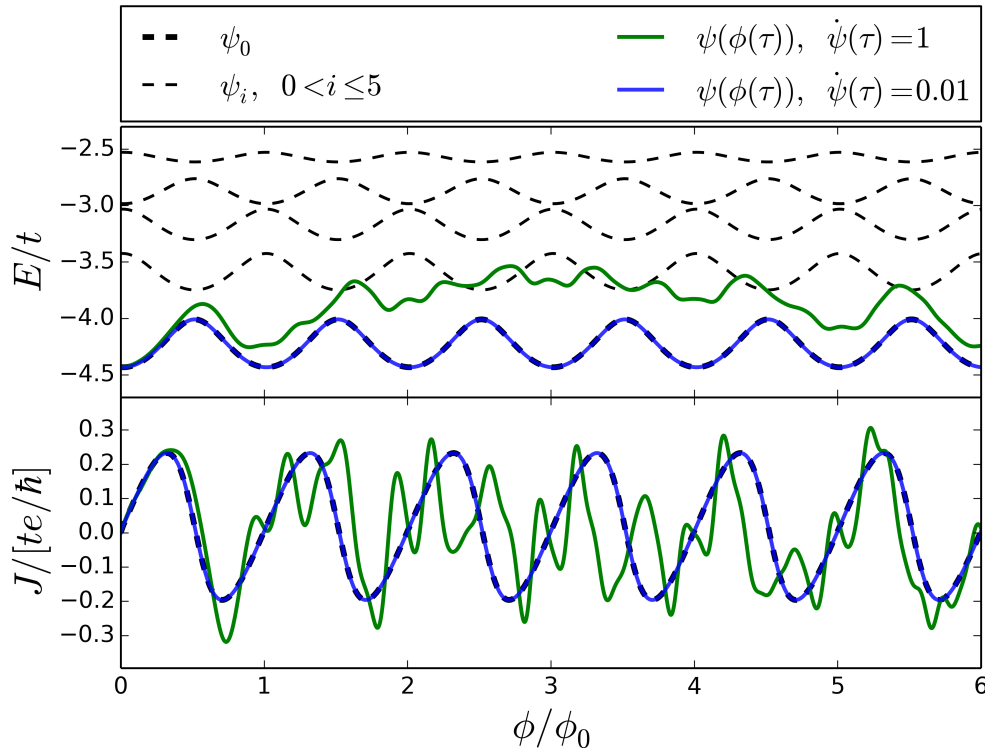


FIGURE 3.5: Steady state, and time-evolution calculated energies and currents of a six site ring at half filling ($N_{\uparrow} = N_{\downarrow} = 3$). Note that the system follows the groundstate calculation for adiabatic, but not for non-adiabatic ramping.

3.3 Quantum rings in the periodic Anderson model

This section presents the results for simulations of the periodic Anderson model. All calculations of the PAM ring system considers a ring of six conduction sites and six impurity sites. The number of electrons here is always 12 with six spin-up electrons and six spin-down electrons.

The first figure (Fig. 3.6) reproduces the spin-spin correlations from a study by Luo et al. [7]. The figure illustrates a key aspect of the periodic Anderson model, namely the competition between Kondo spin coupling and RKKY spin-ordering. At low values of the Hybridization parameter V , the electrons in the conduction band are free and able to work as links between the impurities, which means that the RKKY-interaction becomes stronger. For higher values of V on the other hand, the Kondo spin coupling becomes stronger and electrons are becoming more localized to the specific sites.

The competition between RKKY and Kondo is seen clearly in the spin-spin correlations presented in figure 3.6; a high negative spin-spin correlation between a conduction site and the connected impurity site implies strong Kondo spin coupling, and high negative spin-spin correlation between neighboring impurity sites implies a strong RKKY-interaction. When the spin-spin correlations between conduction and impurity sites are stronger than that of neighboring impurity sites, the system is said to be in the Kondo regime or Kondo phase, and when the opposite is true, the RKKY regime or RKKY phase.

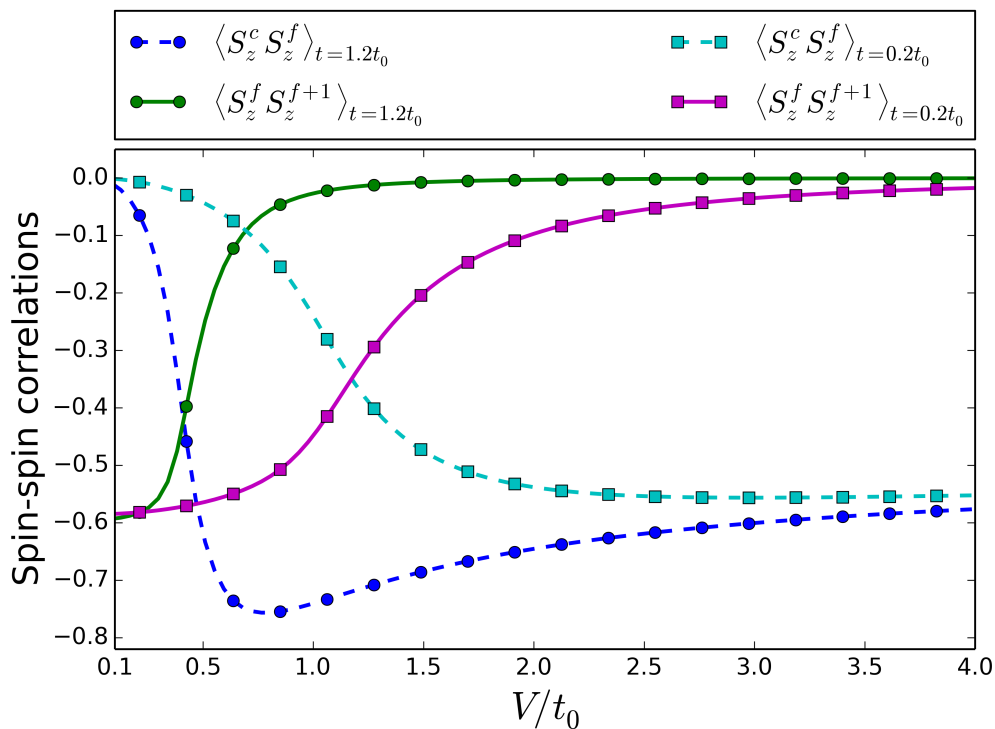


FIGURE 3.6: Reproduced results from Luo et al. 2005 [7]. Circles are referring to $t = 1.2t_0$ and squares to $t = 0.2t_0$ with $t_0 = 1$ being the energy unit. $U/t_0 = 5$ in both cases.

The different phases of the system can depend on a number of parameters, and a diagram displaying the phase depending on such parameters is called a Doniach phase diagram.

One example of a Doniach phase diagram can be found the same paper by Luo et al. [7], where a Doniach phase diagram is presented in the temperature-Hybridization plane. In figure 3.7 a Doniach phase diagram in magnetic flux-Hybridization plane is presented. We can see that for every value of ϕ , the same qualitative behavior of figure 3.6 is reproduced, that is, Kondo correlations increase and RKKY correlations decrease with increasing Hybridization. Furthermore, the crossover behavior where the system goes from the RKKY- to the Kondo-regime can be observed. For the case of a magnetic field piercing the ring, it is clear that the value of Hybridization where this crossover occurs depends on the strength of the magnetic field, and a maximum of the Kondo correlations can be seen at $\phi = 0.5\phi_0$.

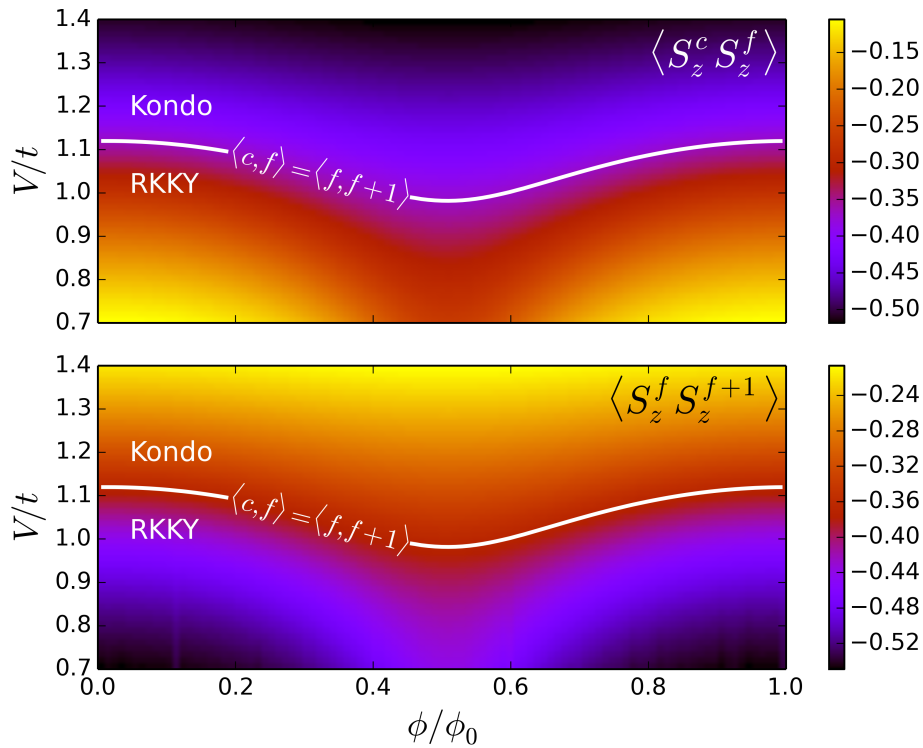


FIGURE 3.7: Doniach phase diagram in the (V, ϕ) -plane for a six site PAM ring. $\langle i, j \rangle$ is short notation for $\langle S_z^i \cdot S_z^j \rangle$. Note how the Kondo correlations ($\langle S_z^i \cdot S_z^j \rangle$) are stronger close to $\phi = 0.5 \cdot \phi_0$.

In figure 3.8 we see the persistent current of the same system as in figure 3.7. Note that the values of V now extend to zero in the lower bound. The current displays a clear dependence on the Hybridization parameter, and for large values of V the current essentially dies out. This behavior can be explained by the formation of Kondo singlets, that is, for large values of V , it is more energetically favorable for the electrons to stay close to the impurities instead of spreading out over the ring. In contrast, for low values of V , the electrons are more likely to spread out, and for the extreme case $V = 0$ the

impurities are completely cut-off from the ring. The current for that case assumes the same behavior as for the 1D-ring without impurities in figure 3.4. The same behavior can be seen for $U \rightarrow \infty$, as the electrons of the impurities become highly localized, and cut-off from the ring as well.

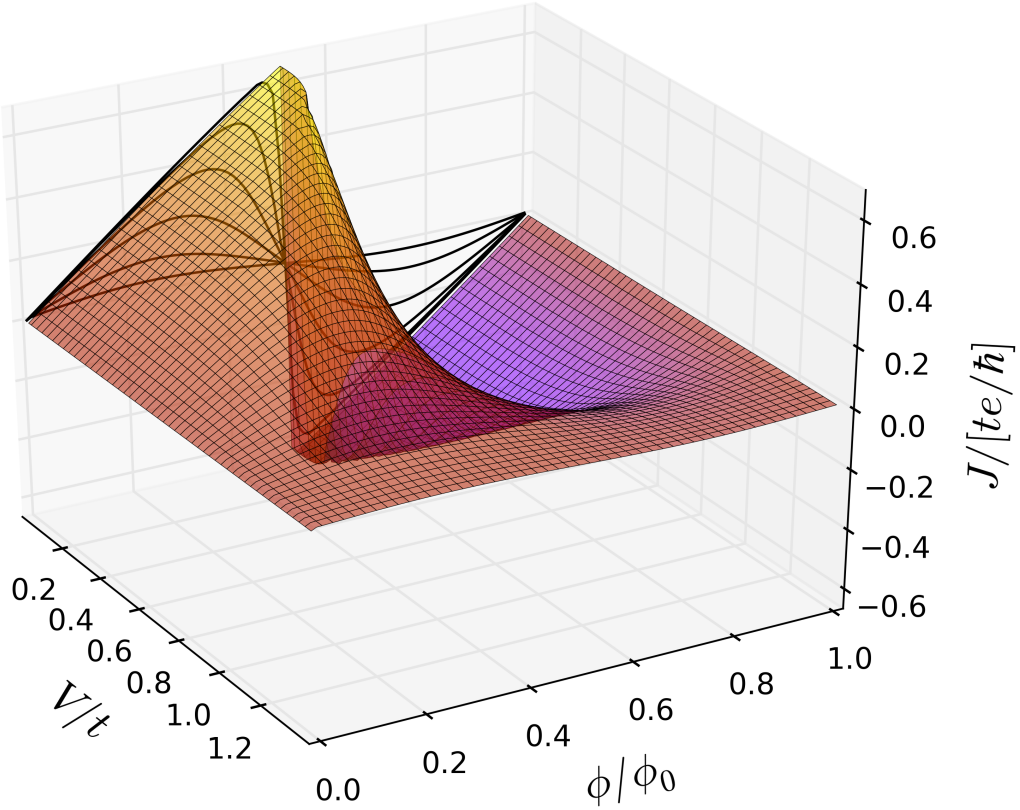


FIGURE 3.8: Groundstate persistent current of a six site PAM ring for different values of the Hybridization, V , and the magnetic flux, ϕ . At $V = 0$ the impurity sites are completely cut-off from the ring and the current becomes the same as in a pure six site ring.

Figure 3.8 also shows a clear difference in the current dependence of V , for different values of the magnetic flux. If, for instance, the case of $\phi = 0.2\phi_0$ is compared to $\phi = 0.4\phi_0$, it is clearly seen that the current drops much faster and much earlier for the higher flux. This behavior is in line with the earlier crossing from RKKY to the Kondo regime, as was seen in figure 3.7. This crossover behavior can also be seen looking at entanglement.

Figure 3.9 shows the concurrence between conduction and impurity-sites, and between neighboring impurity sites. The concurrence between conduction and impurity sites C_{cf} displays essentially the same behavior as the spin-spin correlations, that is, the entanglement is maximized at $\phi = 0.5\phi_0$. Since the concurrence is maximized for a singlet state, we can interpret that the increase is due to formation of Kondo singlets.

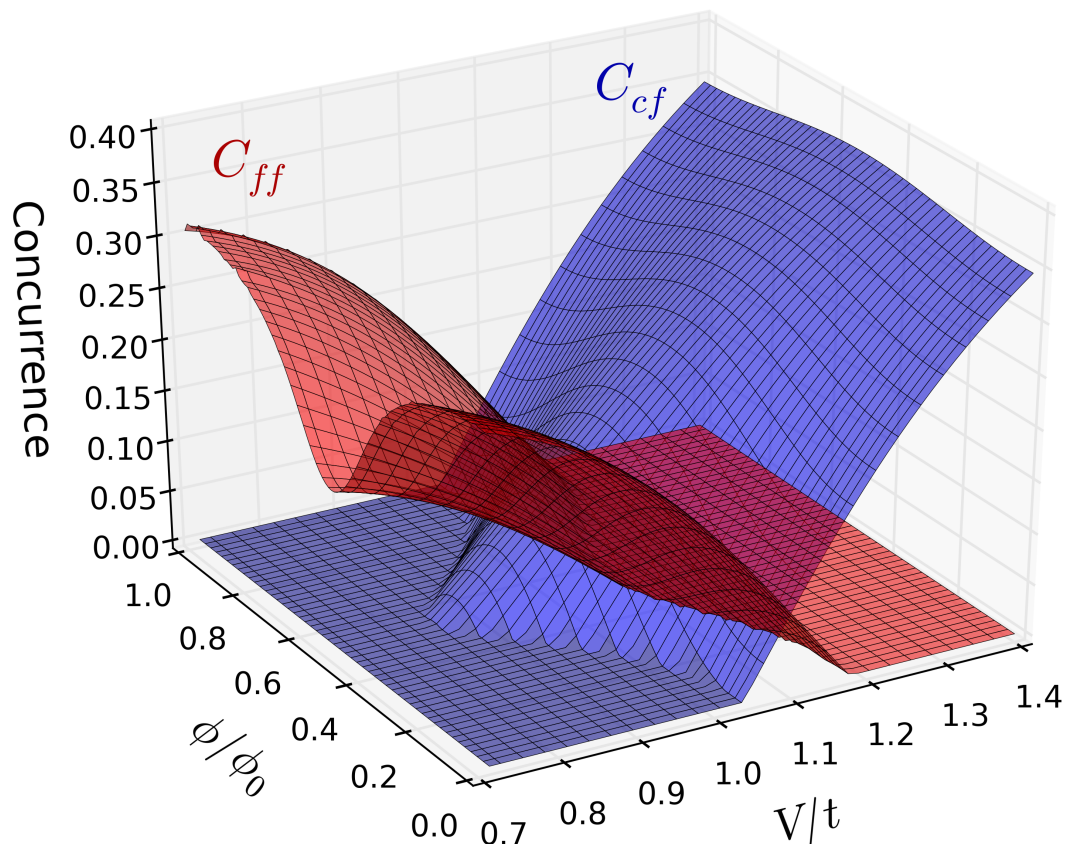


FIGURE 3.9: Entanglement, measured in terms of concurrence, between the conduction and impurity sites, C_{cf} , and neighboring impurity sites, C_{ff} . Notice how the entanglement is, minimized at $\phi = 0.5 \cdot \phi_0$ between neighboring impurity sites is, and maximized between conduction and impurity sites.

The concurrence between neighboring impurity sites is also in line with the spin-spin correlations in figure 3.7.

The reason why Kondo correlation effects are stronger near $\phi = 0.5\phi_0$ is not clear, and further investigations are ongoing.

3.3.1 Local magnetic field

Here we consider the same PAM ring as in the previous subsection, but with the addition of a local magnetic field at one of the conduction sites. The field is assumed to be in the z -direction, and it results in the following Zeeman term:

$$H_Z(\tau) = g\mu_B B_z(\tau) S_z. \quad (3.4)$$

We consider the case of a strong magnetic pulse,

$$B_z(\tau) = \begin{cases} 0 & \text{if } \tau \leq 0 \\ 2 & \text{if } 0 < \tau \leq 1 \\ 0 & \text{if } \tau > 1 \end{cases} \quad (3.5)$$

The magnetic field here is units of $\frac{t_0}{\mu_B}$ which means that if t_0 is 1eV, the magnetic field will be of order of $\sim 30\text{kT}$ which is far too strong for an experimental realization. However, if $t_0 = 1\text{meV}$ instead, then the field required would be of the order of $\sim 30\text{T}$ which would not require a small neutron star in the laboratory. The results presented here are, however, very preliminary, and should therefore be seen more as a theoretical exploration of the physics of the system instead of a suggestion for experimental work.

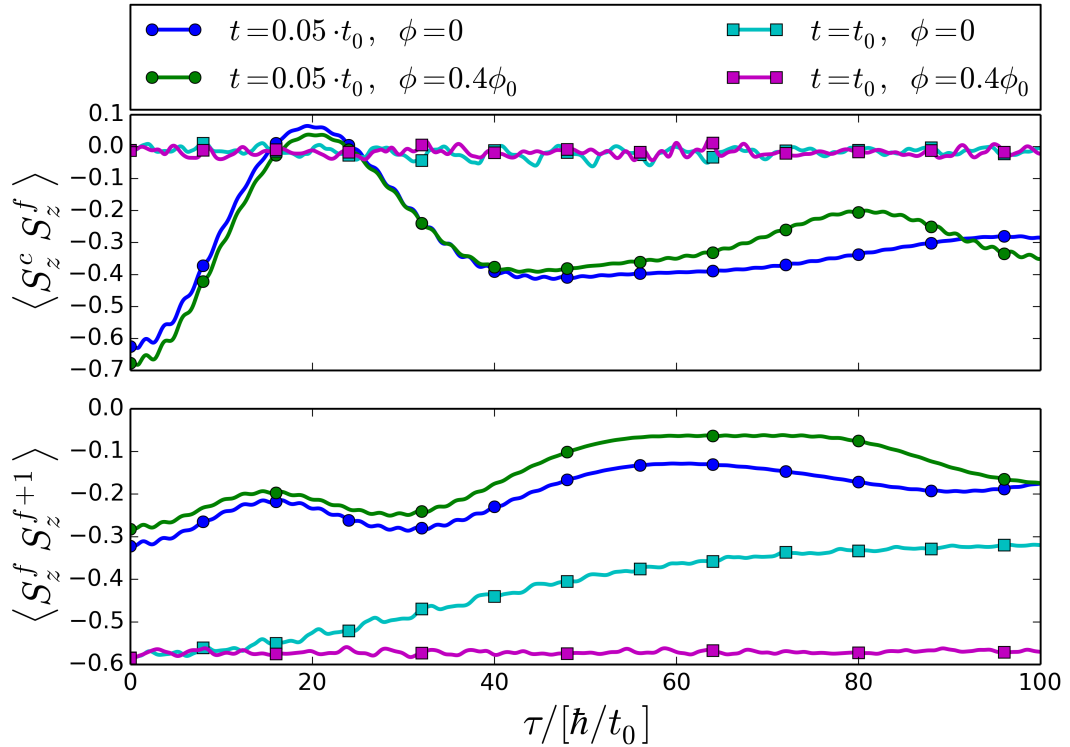


FIGURE 3.10: Spin-spin correlations after a sudden magnetic pulse on one of the conduction sites in a PAM ring. Note that RKKY correlation remains unaffected by the magnetic pulse for the case $t = t_0, \phi = 0.4\phi_0$.

In figure 3.10 the time-evolution of the spin-spin correlations is shown for two different values of the hopping parameter, $t = 0.05t_0$ and $t = t_0$, and for zero and non-zero magnetic flux through the ring. The Kondo correlations are calculated for the Zeeman site and its corresponding impurity, and the RKKY correlations are calculated between the impurity that is linked to the Zeeman site and its neighboring impurity. In the case of

$t = 0.05t_0$ we see that the magnetic field is strong enough to break the Kondo singlet. Even though the local magnetic field is only a short pulse, it affects the Kondo correlations for long times, and the correlations do not seem to return to their groundstate values. A likely explanation for this is that the spin-currents (see fig. 3.11) induced by the magnetic pulse are continuing to bring "disorder" to the system even after the the magnetic field is removed.

For the case $t = 0.05t_0$ there is little difference in the behavior of the system for different values of ϕ . In this respect, $t = t_0$ is much more interesting. Especially the behavior of the RKKY correlations, where the $\phi = 0.4\phi_0$, in contrast to $\phi = 0$, remains more or less unaffected by the field. We do not yet have a satisfactory explanation for this very striking difference, and further investigations are ongoing.

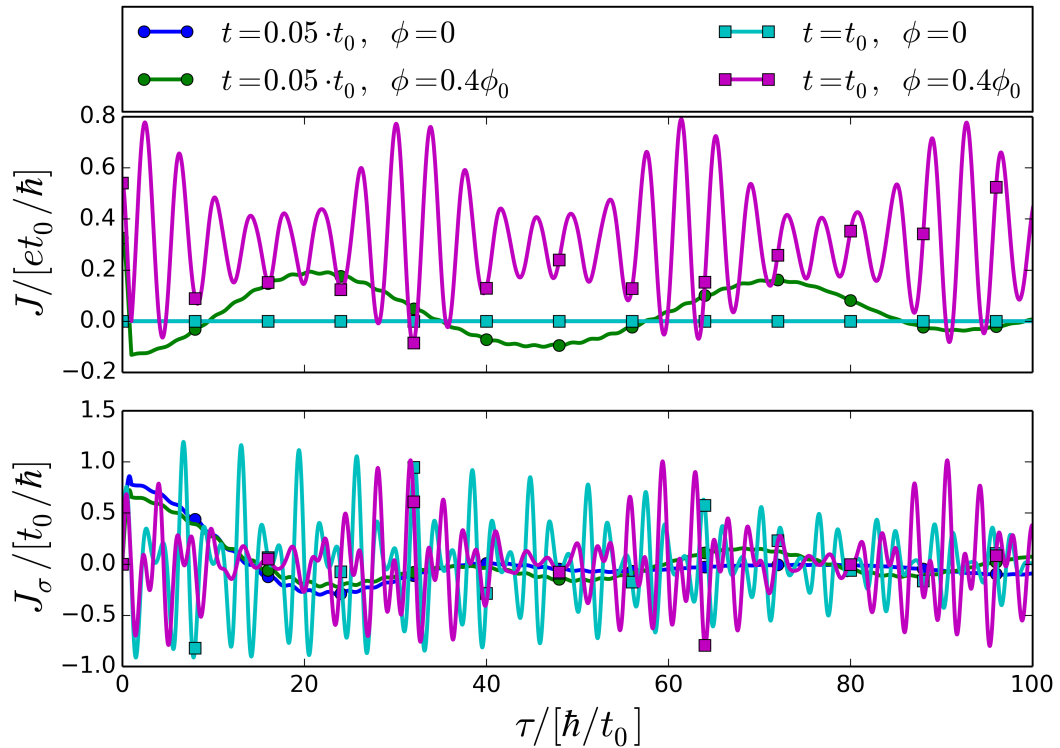


FIGURE 3.11: Charge currents and spin-currents in a PAM ring after a sudden local magnetic pulse. All currents are corresponding to the bond between the conduction site, at which the magnetic field is applied, and the neighboring site. The spin current here is simply the density current of spin up electrons subtracted by the density current of the spin down electrons.

Figure 3.12 presents the Kondo and RKKY correlations, but in this case even for sites further away from the site which is subjected to the local magnetic field. We can see that the local disturbance in the correlations propagates through the ring. Both the RKKY and Kondo correlations become weaker, at least at longer times. The Kondo

and RKKY correlations seem to oscillate with the same periodicity as the spin current (fig. 3.11). It is therefore most likely that the big changes in correlations are due to the spin-current in the ring, and not to oscillations between the conduction sites and their respective impurity. These oscillations is probably what is seen in the correlations connected to the Zeeman site.

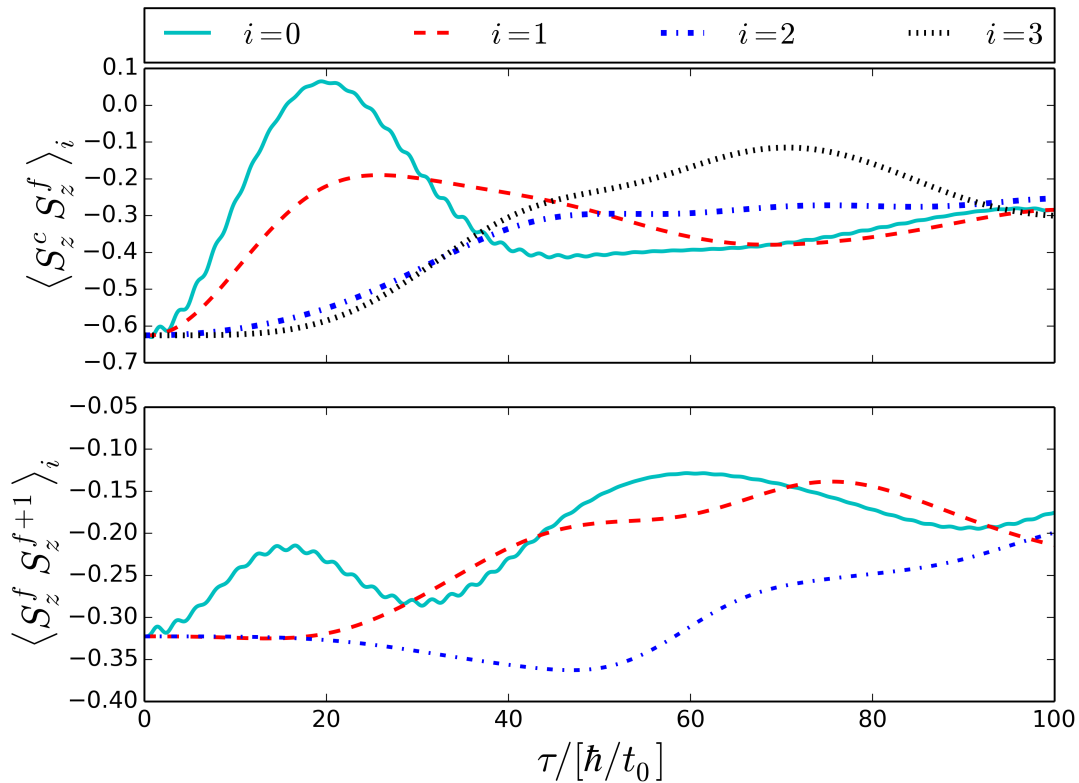


FIGURE 3.12: Spin-spin correlations after a sudden magnetic pulse on one of the conduction sites in a PAM ring. The notation $\langle S_z^c S_z^f \rangle_n$ refers to the Kondo correlations at site n with $n = 0$ being the site of the magnetic pulse. For the RKKY correlations $\langle S_z^f S_z^{f+1} \rangle_n$, n corresponds to the site of the first impurity.

It should be stressed that the results for the Zeeman perturbation are very preliminary, and that further investigations are needed to draw more general conclusions. An interesting extension to this procedure would be to have a magnetic field in the (x, y)-plane instead of in the z-direction. Such a field can however not be used in the current implementation of the computer program, and further development will be needed.

Chapter 4

Conclusions and Outlook

The main objective of this thesis was to investigate magnetization dynamics in quantum rings, in connection to electron-electron spin interactions. An important goal of the thesis was to develop and test an exact diagonalization program. This testing was done, partly using a t-DMRG program and partly using another already tested exact diagonalization program. During the thesis work the same t-DMRG program was used in another project. The collaboration in that project, which consisted of providing t-DMRG results as benchmarks, has resulted in the co-authorship of a paper (that will be submitted in the next few weeks) presenting a novel many-body approximation method. The exact diagonalization program has, aside from being tested against the t-DMRG program, also reproduced several results from the literature.

The program, written in Python, makes use of a popular package for quantum simulations in Python, called QuTiP. The use of QuTiP has provided a good overall structure to the program, and it opens up for the inclusion of many new features available in QuTiP, for example: absorbing boundary conditions, quantum optimal control theory and Quantum Monte Carlo simulations. The time-evolution procedure of the program was written using two very commonly used packages for scientific Python, namely Numpy and Scipy. Although written in Python, the time-evolution procedure is as fast as another implementation of the same algorithm written in Fortran. Both of these procedures outperform the exact time-evolution procedure available in QuTiP when it comes to large systems.

The thesis has, using the exact diagonalization program, shown how the persistent currents in a periodic Anderson model ring, change with respect to a piercing magnetic flux ϕ and the hybridization V between the conduction and impurity sites. Along with these results, a Doniach-type phase diagram in the (ϕ, V) -plane is provided. The results

show that the Kondo correlations and RKKY spin-ordering are dependent on the magnetic flux piercing the ring. Kondo correlations are strongest for a flux close to the half flux quantum. Looking at concurrence, a measure of entanglement, a similar picture is reached; the entanglement between conduction and impurity sites reaches a maximum at $\phi = 0.5\phi_0$. Furthermore, a preliminary investigation is provided was made of how the magnetic state of a PAM ring is affected by a local magnetic pulse on one of the conduction sites.

Despite its exploratory nature, this study offers some insight into the effects of electronic spin interactions in connection to quantum rings. The thesis has shown the behavior of the systems investigated from many different angles, using a variety of observables and quantities (e.g. charge currents, spin-currents, spin-spin correlations and entanglement). Although lacking direct implications for society, this study adds to the collective knowledge of spin-interactions, Kondo physics and quantum rings. These fields are becoming increasingly important, partly because of the prospects of spintronic devices.

There are many possibilities for further investigations. One aspect that could be of interest is the inclusion of spin-orbit coupling in the Hamiltonian. Another possibility could be to extend the Hilbert space, such that the total S_z does not need to be conserved. Through this extension it would be possible to include a Zeeman term that does not restrict the magnetic field to the z -direction.

In conclusion, this thesis studied the persistent currents from quantum rings, together with the Kondo effect and RKKY-interact in the periodic Anderson model. The study has revealed some new interesting results, and it has opened up for many possible further investigations in these very interesting matters.

Bibliography

- [1] G. E. Moore et al. Cramming more components onto integrated circuits, 1965. *Electronics Magazine*, page 4, 1965.
- [2] C. A. Mack. Fifty years of Moore's law. *Semiconductor Manufacturing, IEEE Transactions on*, 24(2):202–207, 2011.
- [3] P. W. Shor and S. P. Jordan. Estimating Jones polynomials is a complete problem for one clean qubit. *Quantum Information & Computation*, 8(8):681–714, 2008.
- [4] M. Adachi, M. Seki, H. Yamahara, H. Nasu, and H. Tabata. Long-term potentiation of magnonic synapses by photocontrolled spin current mimicked in reentrant spin-glass garnet ferrite $\text{Lu}_3\text{Fe}_5\text{Si}_2\text{O}_{12}$ thin films. *Applied Physics Express*, 8(4):043002, 2015. URL <http://stacks.iop.org/1882-0786/8/i=4/a=043002>.
- [5] L. Kouwenhoven and L. Glazman. Revival of the Kondo effect. *Physics World*, page 33, 2001.
- [6] C. Verdozzi, Y. Luo, and N. Kioussis. Disordered Kondo nanoclusters: Effect of energy spacing. *Physical Review B*, 70(13):132404, 2004.
- [7] Y. Luo, C. Verdozzi, and N. Kioussis. Tunable Doniach phase diagram for strongly-correlated nanoclusters. *Physical Review B*, 71(3):033304, 2005.
- [8] P. Samuelsson and C. Verdozzi. Two-particle spin entanglement in magnetic Anderson nanoclusters. *Physical Review B*, 75(13):132405, 2007.
- [9] URL <http://qti.sns.it/dmrg/phome.html>.
- [10] W. J. de Haas, J. H. de Boer, and G. J. van den Berg. *Physica*, 1115(1), 1934.
- [11] J. Kondo. Resistance minimum in dilute magnetic alloys. *Progress of theoretical physics*, 32(1):37–49, 1964.
- [12] C. Krull. Introduction to the Kondo Effect. In *Electronic Structure of Metal Phthalocyanines on Ag(100)*, Springer Theses, pages 31–50. Springer International

- Publishing, 2014. ISBN 978-3-319-02659-6. doi: 10.1007/978-3-319-02660-2_3. URL http://dx.doi.org/10.1007/978-3-319-02660-2_3.
- [13] P. W. Anderson. Localized Magnetic States in Metals. *Phys. Rev.*, 124:41–53, Oct 1961. doi: 10.1103/PhysRev.124.41. URL <http://link.aps.org/doi/10.1103/PhysRev.124.41>.
- [14] J. R. Schrieffer and P. A. Wolff. Relation between the Anderson and Kondo Hamiltonians. *Phys. Rev.*, 149:491–492, Sep 1966. doi: 10.1103/PhysRev.149.491. URL <http://link.aps.org/doi/10.1103/PhysRev.149.491>.
- [15] K. G. Wilson. The renormalization group: Critical phenomena and the Kondo problem. *Rev. Mod. Phys.*, 47:773–840, Oct 1975. doi: 10.1103/RevModPhys.47.773. URL <http://link.aps.org/doi/10.1103/RevModPhys.47.773>.
- [16] P. Nozieres. A Fermi-liquid description of the Kondo problem at low temperatures. *Journal of low temperature physics*, 17(1-2):31–42, 1974.
- [17] S. M. Cronenwett, T. H. Oosterkamp, and L. P. Kouwenhoven. A tunable Kondo effect in quantum dots. *Science*, 281(5376):540–544, 1998.
- [18] U. F. Keyser, C. Fühner, S. Borck, R. J. Haug, M. Bichler, G. Abstreiter, and W. Wegscheider. Kondo Effect in a Few-Electron Quantum Ring. *Phys. Rev. Lett.*, 90:196601, May 2003. doi: 10.1103/PhysRevLett.90.196601. URL <http://link.aps.org/doi/10.1103/PhysRevLett.90.196601>.
- [19] A. Lorke, R. Johannes Luyken, A. O. Govorov, J. P. Kotthaus, J. M. Garcia, and P. M. Petroff. Spectroscopy of Nanoscopic Semiconductor Rings. *Phys. Rev. Lett.*, 84:2223–2226, Mar 2000. doi: 10.1103/PhysRevLett.84.2223. URL <http://link.aps.org/doi/10.1103/PhysRevLett.84.2223>.
- [20] Y. Aharonov and D. Bohm. Significance of Electromagnetic Potentials in the Quantum Theory. *Phys. Rev.*, 115:485–491, Aug 1959. doi: 10.1103/PhysRev.115.485. URL <http://link.aps.org/doi/10.1103/PhysRev.115.485>.
- [21] S. Kasai, T. Niiyama, E. Saitoh, and H. Miyajima. Aharonov-Bohm oscillation of resistance observed in a ferromagnetic Fe-Ni nanoring. *Applied physics letters*, 81(2):316–318, 2002.
- [22] K. Jimenez-Garcia, L. J. LeBlanc, R. A. Williams, M. C. Beeler, A. R. Perry, and I. B. Spielman. Peierls substitution in an engineered lattice potential. *Physical review letters*, 108(22):225303, 2012.

- [23] S. Viefers, P. Koskinen, P. S. Deo, and M. Manninen. Quantum rings for beginners: energy spectra and persistent currents. *Physica E: Low-dimensional Systems and Nanostructures*, 21(1):1–35, 2004.
- [24] S. Doniach. The Kondo lattice and weak antiferromagnetism. *Physica B+C*, 91(0):231 – 234, 1977. ISSN 0378-4363. doi: [http://dx.doi.org/10.1016/0378-4363\(77\)90190-5](http://dx.doi.org/10.1016/0378-4363(77)90190-5). URL <http://www.sciencedirect.com/science/article/pii/0378436377901905>.
- [25] M. A. Ruderman and C. Kittel. Indirect Exchange Coupling of Nuclear Magnetic Moments by Conduction Electrons. *Phys. Rev.*, 96:99–102, Oct 1954. doi: 10.1103/PhysRev.96.99. URL <http://link.aps.org/doi/10.1103/PhysRev.96.99>.
- [26] T. Kasuya. A theory of metallic ferro-and antiferromagnetism on Zener’s model. *Progress of theoretical physics*, 16(1):45–57, 1956.
- [27] K. Yosida. Magnetic properties of Cu-Mn alloys. *Physical Review*, 106(5):893, 1957.
- [28] I. Hagymási, K. Itai, and J. Sólyom. Periodic Anderson model with correlated conduction electrons: Variational and exact diagonalization study. *Phys. Rev. B*, 85:235116, Jun 2012. doi: 10.1103/PhysRevB.85.235116. URL <http://link.aps.org/doi/10.1103/PhysRevB.85.235116>.
- [29] A. Amaricci, G. Sordi, and M. J. Rozenberg. Non-Fermi-Liquid Behavior in the Periodic Anderson Model. *Phys. Rev. Lett.*, 101:146403, Oct 2008. doi: 10.1103/PhysRevLett.101.146403. URL <http://link.aps.org/doi/10.1103/PhysRevLett.101.146403>.
- [30] S. R. White. Density matrix formulation for quantum renormalization groups. *Physical Review Letters*, 69(19):2863, 1992.
- [31] S. R. White. Density-matrix algorithms for quantum renormalization groups. *Phys. Rev. B*, 48:10345–10356, Oct 1993. doi: 10.1103/PhysRevB.48.10345. URL <http://link.aps.org/doi/10.1103/PhysRevB.48.10345>.
- [32] E. M. Stoudenmire and S. R. White. Studying Two Dimensional Systems With the Density Matrix Renormalization Group. *ArXiv e-prints*, May 2011.
- [33] G. Vidal. Efficient Classical Simulation of Slightly Entangled Quantum Computations. *Phys. Rev. Lett.*, 91:147902, Oct 2003. doi: 10.1103/PhysRevLett.91.147902. URL <http://link.aps.org/doi/10.1103/PhysRevLett.91.147902>.
- [34] G. Vidal. Efficient Simulation of One-Dimensional Quantum Many-Body Systems. *Phys. Rev. Lett.*, 93:040502, Jul 2004. doi: 10.1103/PhysRevLett.93.040502. URL <http://link.aps.org/doi/10.1103/PhysRevLett.93.040502>.

-
- [35] S. R. White and A. E. Feiguin. Real-Time Evolution Using the Density Matrix Renormalization Group. *Phys. Rev. Lett.*, 93:076401, Aug 2004. doi: 10.1103/PhysRevLett.93.076401. URL <http://link.aps.org/doi/10.1103/PhysRevLett.93.076401>.
- [36] URL <http://qutip.org/docs/3.1.0/guide/guide-overview.html>. Accessed 2015-06-10.
- [37] C. Verdozzi and C.-O. Almbladh. Lanczos-adapted time evolution for open boundary quantum transport. *ArXiv e-prints*, Aug. 2008.
- [38] G. De Chiara, M. Rizzi, D. Rossini, and S. Montangero. Density Matrix Renormalization Group for Dummies. *eprint arXiv:cond-mat/0603842*, Mar. 2006.
- [39] D. Gobert, C. Kollath, U. Schollwöck, and G. Schütz. Real-time dynamics in spin- $\frac{1}{2}$ chains with adaptive time-dependent density matrix renormalization group. *Phys. Rev. E*, 71:036102, Mar 2005. doi: 10.1103/PhysRevE.71.036102. URL <http://link.aps.org/doi/10.1103/PhysRevE.71.036102>.